Technical University
of Denmark

Thesis

Geothermal Heat Production in Low Permeable Fractured Reservoirs

Student:
Mark Lusty Grandahl
S102918

Supervisors:
Dr. Saeed Salimzadeh
Dr. Hamid M. Nick

Contents

List of Figures

List of Tables

1 Introduction

The global energy consumption has been increasing year after year for decades. Especially Asia has contributed to this growth since the beginning of the 1990's. India alone saw a 4.6% growth in energy consumption in 2016 [1]. This increase can be directly linked to the increasing middle class in these countries, as people get more resources they also start to use more resources. This evolution is not sustainable with traditional fossil fuels, or coal, due to the global warming issue. Therefore, new and clean energy sources have to be used. In 2016, 80% of the energy came from either oil, gas or coal contributing with 32%, 21% and 27% respectively. The remaining 20% came from renewable clean energy sources.
There are several types of renewable energy sources, in which most widely spread are wind, solar and biomass. Different types of renewable energy sources can be found at different locations, since most of them rely on the climate in some way. In Europe sources like wind and hydro can be found in the northern part, and solar is mostly found in the southern part. In the U.S. solar is popular, but also geothermal energy, something not really used in Europe. Not because the conditions to geothermal energy productions is abstinent, but because the public is against the production methods. This means the Europe is missing out on a huge natural energy source, which potentially can limit the dependency on Russian gas, something that has been talked about for many years in Europe.

1.1 Geothermal Energy

Geothermal energy is a renewable clean energy source that is raising in popularity around the world. It refers to the massive amount of energy stored in the crust of the earth, as heat. This heat has been used in centuries, first in the form of hot springs. The most famous example of a hot spring generated by geothermal energy is the blue lagoon located in Iceland. Springs like these were primarily used to bath in or to cook. The first documented geothermal power plant producing electricity was invented in the early 20^{th} century, where the Italian scientist Piero Ginori Conti successfully test a geothermal power plat by turning on four light bulbs using steam to generate the electricity [2]. Even though this is more than a century ago, geothermal energy in 2016 still made up less than 1% of the total energy consumption in the world. [3].
Today geothermal energy is extracted from the earth's crust, by drilling injection and production wells. The so-called doublet system in which cold fluid (i.e. water) is injected at the injection well and the hot water or steam is produced from the production well, is very popular in geothermal sites around the world. Thus, in this work the focus will be on a doublet system. These types of systems rely on the injected fluid being able to flow from the injection well to the production well through the reservoir, either using the natural permeability of the formation or fractures in the formation as flow paths. Geothermal systems is often found in shallower reservoirs with a high temperature where the permeability of the formation is high enough for the fluid to flow from the injection well to the production well. These types of systems are often found in locations where the subsurface is heated by volcanic activity, places like Iceland are a prime example of this.
Geothermal heat can be used in two different forms. Either the energy from steam or hot water produced from the reservoir can be transformed into electricity using a generator, or the hot produced water can be fed directly into the district heating system and used to heat buildings.

1.2 Enhanced Geothermal Systems (EGS)

In most places the temperature needed for a geothermal energy system to be efficient is very deep in the subsurface. This presents other challenges, the main one being that the natural permeability of the formations deep in the earth's crust is too low for the fluid to flow efficiently and economically. Therefore, these systems strongly rely on fractures in the formation to sustain the fluid flow between the wells. If these fractures don't exist naturally in the formation they have to be induced or engineered so that the flow through the reservoir is enhanced. These systems are so-called Enhanced Geothermal Systems (EGS). There are several ways to create manmade fractures. The most common used methods are hydraulic and acid fracturing. In hydraulic fracturing, a fluid is injected at a pressure high enough to break the formation. In acid fracturing, a corrosive fluid, depending on the properties of the formation, is injected to the formation to dissolve the rock minerals and create wormholes and flow paths. These methods have been used both in the oil industry to enhance production and in geothermal industry, but a new way called radial jet drilling is starting to gain momentum, it is already used in the oil and gas industry with good results.

1.3 Fracturing

Several methods can be used to fracture the rock. The most common ways are acid fracturing, thermal fracturing and hydraulic fracturing.
Acid fracturing [4] is best suited for low temperature conditions. This is because that high temperatures increase the rate the acid reacts with the rock. So, for high temperatures the acid won't have time to propagate far into the formation before the reaction is complete. The reaction rate between the injected acid and the formation can be slowed down by adding chemicals to the acid. These chemicals however, are very expensive. So, this option is rarely chosen. Various types of acid is used for acid fracturing, some of the most used is hydrochloric acid (CHl) with concentration varying from 15 % to 28 %, formic acid ($HCOOH$) and acetic acid (CH_3COOH)
Thermal fracturing is where cold water is injected into the reservoir and cools the formation. Thus, the formation contracts and fractures will occur as a consequence of this contraction. An important thing to consider when using thermal fracturing is the in-situ stresses, and how the well is placed with respect to the in-situ stress state. If the well is placed wrong in relation to the in-situ stresses it can lead to a very high risk of well instability within a very short time after production is started.
Hydraulic fracturing is where a fracking fluid is used to create new fractures in the formation. This is done by injecting a fluid (usually water with some sand added). The sand stays in the fracture after the fracking process and makes sure that the newly created fractures won't collapse in on itself after the pressure is removed. It is a widely used well stimulation technique. It was used the first time in 1947 as an experiment, and was commercially used for the first time in 1950 [5].
The use of hydraulic fracturing is very controversial, especially in European countries. The people in favor of fracking highlights the economic benefits of more difficult reservoirs becoming posible to produce. The people not in favor of hydraulic fracturing emphasize the environmental impacts such as the risk of ground water contamination and the possible triggering of earthquakes [6].

1.4 Radial Jet Drilling (RJD)

Radial Jet Drilling (RJD) is a technique where high velocity fluids is used to drill micro-holes from an excising well. This technology became increasingly popular between 2000 and 2008 due to the almost

constant increase in the oil price. This meant that new technologies became increasingly popular to maximize the recovery in the oil and gas industry, hence the development of the lateral drilling technique. This technology has since been adopted to other fields then just oil production. The geothermal industry has begun to use the technology to increase the flow paths between the injection well and the production well. A limiting factor on this technology is the drillable length of these micro-holes [14] looked into this, and found an expression for the maximum drillable length, and found that the dominating factor on the drillable length was the flow rate. The biggest advantage of RJD over the more traditional way of creating fractures is its ability to bypass any collapsed or damaged zone surrounding the well bore.
The setup needed to create laterals from an existing well is quite simple. Figure 1 shows the setup used to drill micro-holes from an existing well.

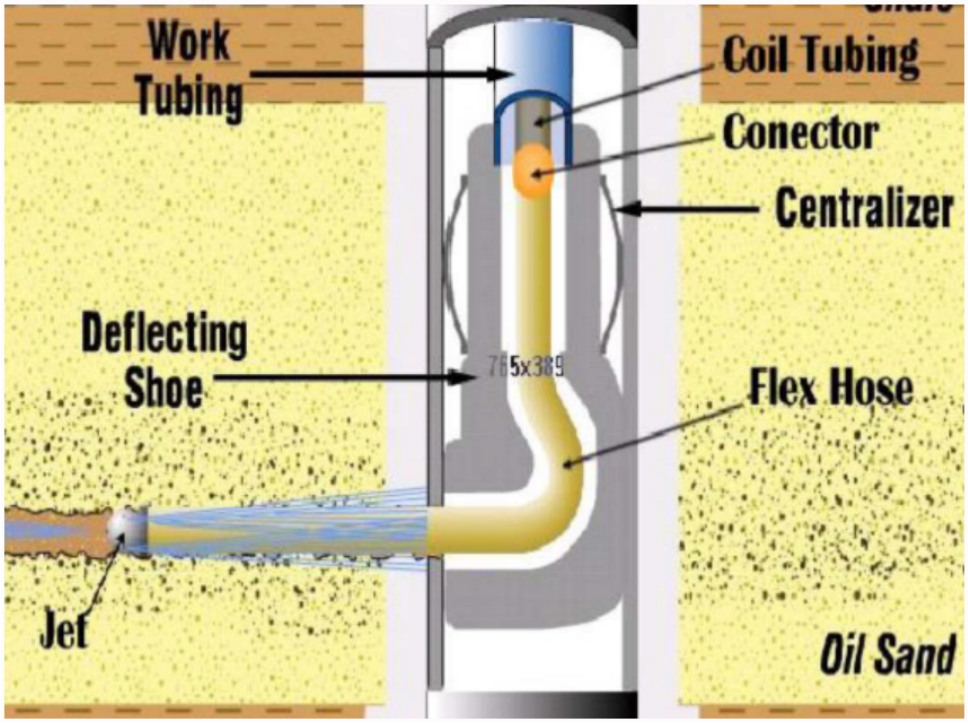

Figure 1: Setup for radial jet drilling.

A deflecting shoe is lowered into the well using a work tubing working as a casing for the rigid coil tubing. At the end of the coil tubing the flexible hose is attached. To the other end of the flexible hose the drilling nozzle is attached. When the high-pressure fluid is applied the flexible hose will extend, and follow the drilling nozzle into the formation. [14] looked into the force balance of the RJD system, the only force providing forward motion is the backward facing nozzles. This force has to overcome the counteracting friction forces from the flexible hose moving through the deflecting shoe, the flexible hose moving in the annulus of the lateral and the force between the flexible hose and the fluid flowing in the annulus. The last one is usually neglected in the force balance due to it being very small compared to the other contributing forces.
Water is most commonly used in RJD, but in some cases it is not an option to use water. This can be in water-sensitive formation where water isn't an option due to the risk of swelling. In such cases diesel is the natural alternative to use. After the lateral has been drilled using the pressurized fluid. RJD's are very flexible, as they can be made everywhere in a given well. They aren't limited to the bottom of

the well. The direction of the lateral is also controllable by changing the orientation of the deflection shoe used to steer the jetting nozzle. Laterals has an approximate diameter between one and two inches. Due to the flex hose not being rigid, it is difficult to control the direction of the nozzle once inside the formation. The nozzle will always follow the path of least resistance though the formation. The nozzle used for RJD both use high pressure fluid to cut the rock in front, and to propel itself into the formation. Figures 2 and 3 shows a cross section and the front of such a nozzle respectively.

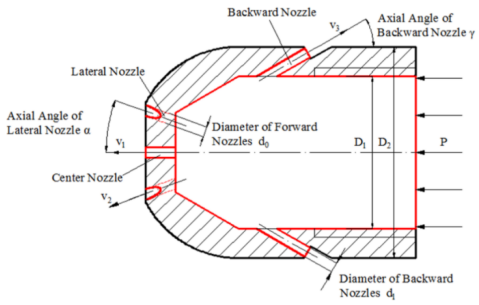

Figure 2: A cross section view of a nozzle.

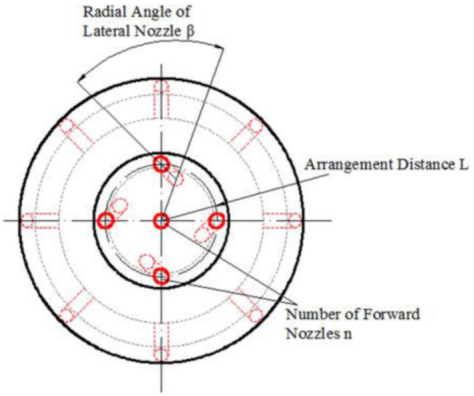

Figure 3: The front of the nozzle.

Another important factor when using RJD's beside the length of the lateral is the pattern of which they are created. [15] looked into the pattern of the laterals, and found that the optimal pattern for a system with four laterals was with a 90° spacing. Therefore, this pattern will be used throughout this work.

1.4.1 Radial Jet Drilling in Geothermal Reservoirs

RJD mainly have their using in Enhanced Geothermal Systems (EGS) where the natural permeability of the reservoir is low, and the connectivity between the injection well and the production well is low. Here RJD's can be used to enhance the flow paths between the wells by connection the wells to some natural fractures in the reservoir. In this case the number of micro-holes drilled has a large impact on the improved productivity. This was shown by [15] and [13]. This technique could in the future be used instead of the older fracking methods such as acid fracturing or thermal fracturing.
When looking at it that way, this technology has the potential to restart the geothermal energy sector in Europe, which has been at a low point for quite some years now. Mainly due to the public resistance to the conventional fracking methods used today.

1.5 Coupled THM Models

The modelling of EGS is very complex, several methods have been used over time to model EGS. Some of these methods include the Finite Element Method (FEM), Finite Volume Method (FVM), Finite Difference Method (FDM), Displacement Discontinuity Method (DDM) and the Boundary Element Method (BEM) which is based in the Boundary Integral Equation (BIE). McClure & Horne, (2014) [25] Used the DDM to simulate the stresses caused by the deformation of the fluid caring fracture, under the assumption of homogeneous, isotropic and linear elastic deformation. [24] They showed that the equations used in the DDM when solving 3D crack problems is the same as those used in the BEM. They showed that the DDM method is better suited for flat fractures, since it uses a local coordinate system on the fracture. So, if used on curved fractures, or fractures of different orientations some modifications are needed. Whereas

the BEM which is based on the BIE can be applied to more general case. Crooijmans et al. (2016) [16] used the FEM approach to investigate the effect of reservoir heterogeneity on the expected lifetime of a geothermal reservoir, the energy recovery rate at various discharge rates. The geothermal reservoirs lifetime was estimated using the Net-to-Gross ration (N/G). Sanyal & Butler (2005) [28] Used the FDM approach to evaluate sub commercial reservoirs, and the vertical fractures spacing needed to the project economical feasible.

Analytical modelling of EGS is used when the reservoir is very well defined, and preferable some symmetry is found in the modelling domain. Bodvarsson (1969) [12] Presented an analytical solution for the 1D heat transfer between rock and fluid for fluid flow in a single fracture. As a function of the distance from the injection point into the fracture, the distance perpendicular to the fracture surface and the time since injection begun. [20] Presented an analytical solution for the fluid temperature as a function of the radial distance from the injection point, the distance the fluid has travelled into the formation perpendicular to the fracture plan, and the time since the cold water injection was begun.

Most EGS modelling is done using numerical modelling methods. Because when modelling EGS, a coupled prosses of Thermal, Hydrological, Mechanical and Chemical (THMC) has to be considered Ghassemi and Zhou, (2011) [21]. Therefore, it is always preferred to include all four parts in the modelling, however this can be difficult. So, in this study the chemical effects are ignored, and a coupled Thermal, Hydrological and Mechanical model (THM) is used. This type of model has been widely used to model EGS. Ghassemi and Zhou, (2011) [21] studied the response of the fractures using a coupled THM model, they modelled the fluid flow and heat transfer within the fracture using the Finite Element Method (FEM), and found that in the early injection state the fracture aperture and pressure is dominated by the poroelastic effects. After a long time with fluid injection the thermoelastic stress becomes the controlling factor for the fracture aperture and pressure. They also studied the effect of fluid leak off from the fracture to the formation and found that a large leak off of fluid into the formation resulted in a decrease in fracture aperture and pressure compared to the case with a low leak off. Pandey et al. (2017) [26] compared a THM and a TH model to determine the effect of the mechanical reactions on a EGS, and found that a TH model strongly overestimates the potential of a EGS. The reason for this is that the fracture aperture in a TH model is kept constant, and won't grow over time. Whereas the fracture aperture grows over time which leads to increased flow through the fracture, and thereby a shorter breakthrough time. [23] used a coupled THM 2D model to simulate flow in a single fracture, they used the a non-linear joint law to determine the describe the hydraulic aperture of the fracture as a function of the normal stresses. They found that a reduction in the normal stress will result in a larger fracture aperture, and thereby a increase in production rate. The difference in normal stress was made by ignoring the effect of thermo-elasticity in one of the simulations, everything else was kept the same. Ekneligoda and Min Ki-Bok, (2014) [18] looked into the effect of flow rate, fracture width and fracture spacing in the vertical plane. They found that the production temperature strongly depends on all three parameters, they tested two different flow rates 20 kg/s and 40 kg/s. The fracture was modelled as permeable layers surrounded by impermeable layers representing the rock formation, the fracture aperture used in this study was 0.01 m. They also tested the minimum half spacing between the fractures to avoid thermal interference between independent fractures against the analytical solution given by Bodvarsson and found that the minimum half spacing for a mass flow rate of 40 kg/s for a 5 year production period the half spacing between fractures should by greater than 20 m, and for a 10 year production period the half spacing should be greater than 30 m. Williems et al., 2017 [29] investigated the effect of well spacing in a doublet system geothermal reservoir. Sanyal & Butler (2005) [28] investigated a sub-commercial reservoir using three different well patterns, a doublet system, a triplet system (one injection well and two production wells) and a five-spot system (one injection

well and four production wells). They stimulated the rock with manmade fractures in different heights of the reservoir to find the minimum distance needed to make the reservoir economical feasible. They also performed a sensitivity analysis, and found that the cooling rate of the produced fluid over times isn't the main criteria for determining the efficiency of a EGS. It is fairer to look at the net generation profile over the life time of the project, and the reservoir heat recovery factor. They also proved that improving the permeability of a reservoir, without increasing the matrix-to-fracture heat transfer area will have little to no benefit on the heat recovery or the net generation.
In this study the effect of Radial Jet Drilling (RDJ) on the production parameters of a geothermal reservoir. The main parameters that will be studied is how the laterals created by RJD effect the thermal draw down of the reservoir, the break through time of the cold-water front and the effect on the down hole pressures of the wells. Furthermore, the effect on these parameters will be looked at from an economical perspective.

2 Computational Model

The heat recovery from a geothermal reservoir is dependent on the circulation of a fluid with a temperature lower than the reservoir. The heat recovery process is a complex process that can be described as several isolated processes all contributing to the heat recovery of the system. The heat recovery process can be described using five sub-models each describing an isolated process. These five models describe the fluid flow through the rock matrix and the fracture, the heat transfer through the rock matrix and the fracture, and the mechanical deformation of the rock matrix.

A fully coupled thermoporoelastic model for modelling discrete fractures in a deformable medium is presented by Salimzadeh et al. (2018a,b). A three-dimensional domain is modelled, and within that the fractures are modelled as discontinuous surfaces. In specific cases when certain conditions are met the fully coupled model can be decoupled to two models. One for solving the mechanical deformation and the contact tractions (M), and one for solving the non-isothermal flow through the 3D domain containing the fractures (TH) Salimzadeh et al., 2018b.

When only using a TH model the fracture aperture a_f is treated as a constant, but when using a THM model the Barton-Bandis model [10, 11] is used to evaluate the fracture aperture at each time step.

$$a_f = a_0 - \frac{a\sigma_n}{1 + b\sigma_n} \tag{1}$$

where a_0 is the maximal fracture aperture when the contact stress is zero, σ_n is the normal contact stress and a and b are model parameters.

2.1 Governing Equations

The fully coupled model consist of five sub-models, two for the fluid flow through the rock matrix and the fractures, two for the heat transfer of the rock matrix and the fractures, and one for the solid deformation of the rock matrix. Below the governing equations for these five processes are defined.

Matrix Flow

The flow of fluid through a porous medium can be defined by combining the mass conservation of the fluid with Darcy's law defining the velocity of the fluid. The mass balance for a fluid in a well defined volume is defined as

$$div(\rho_f \phi v_m) + \frac{\partial}{\partial t}(\rho_f \phi) = 0 \tag{2}$$

The Darcy velocity of a single phase flow in a porous medium is defined as

$$v_f = -\frac{k_m}{\mu_f}(\nabla p_m + \rho_f g) \tag{3}$$

The fluid flow through the rock matrix is solved for every time-step in the simulations using equation 4.

$$div\left[\frac{\mathbf{k}_m}{\mu_f}(\nabla p_m + \rho_f \mathbf{g})\right] = \left(\frac{\alpha^2}{K} + \phi c_f + \frac{\alpha - \phi}{K_s}\right)\frac{\partial p_m}{\partial t} + \phi(\beta_s - \beta_f)\frac{\partial T_m}{\partial t} \tag{4}$$

Fracture Flow

The flow of fluid through a fracture in a reservoir is governed by the mass conservation of the fluid and the cubic law used to define the velocity of the fluid through the fracture. The mass balance in a fracture is defined as

$$div(a_f \rho_f v_f) + \frac{\partial}{\partial t}(a_f \rho_f) = 0 \tag{5}$$

The velocity of the fluid in the fracture is defined using the cubic law

$$v_f = -\frac{a_f^2}{12\mu_f} \nabla p_f \tag{6}$$

The fluid flow through the fractures is solved for every time-step in the simulations using equation 7.

$$div\left(\frac{a_f^3}{12\mu_f} \nabla p_f\right) = \left(\frac{1}{K_n} + a_f c_f\right) \frac{\partial p_f}{\partial t} - a_f \beta_f \frac{\partial T_f}{\partial t} \tag{7}$$

Matrix Heat Transfer

The heat transfer between the rock matrix and the fluid in the rock matrix is solved for every time-step in the simulations using equation 8.

$$div(\lambda_m \nabla T_m) = (\rho_m C_m - \beta_s^2 K T_m) \frac{\partial T_m}{\partial t} - (\alpha \beta_s + \phi \beta_f) T_m \frac{\partial p_m}{\partial t} + \rho_m C_m \mathbf{v}_m \nabla T_m \tag{8}$$

Fracture Heat Transfer

The heat transfer between the rock matrix and the fluid in the fractures is solved for every time-step in the simulations using equation 9.

$$div(a_f \lambda_f \nabla T_f) = a_f \rho_f C_f \frac{\partial T_f}{\partial t} - a_f \beta_f T_f \frac{\partial p_f}{\partial t} + a_f \rho_f C_f \mathbf{v}_f \nabla T_f \tag{9}$$

Mechanical Deformation

The mechanical deformation of the rock matrix is solved for every time-step in the simulations using equation 10.

$$div(\mathbf{D}\epsilon) + \mathbf{F} = div(\alpha p_m \mathbf{I}) + div(\beta_s K (T_m - T_0)\mathbf{I}) \tag{10}$$

Where $\mathbf{k}_m$ is the intrinsic permeability tensor of the rock matrix, ϕ is the porosity of the rock matrix, α is the Biot coefficient, K is the bulk modulus of the rock matrix, K_s is the bulk modulus of the rock matrix when not saturated with a fluid, k_n is the is the intrinsic permeability of the rock matrix in the direction normal to the fracture, μ_f is the viscosity of the fluid, ρ_f is the density of the fluid, ρ_m is the density of the rock matrix, β_s is the volumetric thermal expansion coefficient of the rock matrix, β_f is the volumetric thermal expansion of the fluid, K_n is the fracture tangent stiffness, C_m is the rock matrix heat capacity, C_f is the fluid heat capacity, λ_m is the average thermal conductivity of the rock matrix, λ_f is the average thermal conductivity of the fluid, λ_n is the average thermal conductivity of the rock matrix along the direction normal to the fracture, T_0 is the initial temperature of the rock matrix, T_m is the temperature of the rock matrix, T_f is the temperature of the fluid, p_m is the fluid pressure in the rock matrix, c_f is the fluid compressibility factor, $\mathbf{n}_c$ is the normal vector to the fracture plan, $\mathbf{v}_m$ is the fluid velocity in matrix, $\mathbf{v}_f$ is the is the fluid velocity in fracture, $\mathbf{D}$ is the drained stiffness matrix, ϵ is the strain, $\mathbf{F}$ is the body force per unit volume, $\mathbf{I}$ is the second-order identity tensor and $\mathbf{g}$ is the gravitational constant.

2.2 Finite Element Method (FEM)

The principle behind the Finite Element method (FEM) is to divide a larger volume into smaller sub-volumes and make calculations for each sub-volume, and the interactions between neighboring sub-volumes.

The governing equations behind the solver described in section 2.1 are solved using FEM. In this process the Finite Difference Method (FDM) [9] is used for temporal discretization, and Galerkin's method [8] are used for spatial discretization. The main variables in this process is the fluid pressure of the fluid in the matrix p_m and in the fracture p_f, the temperature in the matrix T_m and in the fracture T_f together with the displacement vector $\mathbf{u}$. Using the standard notation for the Galerkin method these variables can be approximated for each element as

$$u = \mathbf{N}\hat{u} \tag{11}$$

$$p_m = \mathbf{N}\hat{p}_m \tag{12}$$

$$p_f = \mathbf{N}\hat{p}_f \tag{13}$$

$$T_m = \mathbf{N}\hat{T}_m \tag{14}$$

$$T_f = \mathbf{N}\hat{T}_f \tag{15}$$

where $\mathbf{N}$ is a vector containing the shape functions. This can also be written as $X = \mathbf{N}\hat{X}$ where X is a vector containing the all the main variables $X = \{u, p_m, p_f, T_m, T_f\}$ and $\hat{X}$ contains the nodal values of the same variables. Using the FDM the time derivative of the variables in the vector X can be defined as

$$\frac{\partial X}{\partial t} = \frac{X^{t+dt} - X^t}{dt} \tag{16}$$

where X^t and X^{t+dt} are the values of the variables in the vector X to the time t and $t+dt$, respectively. The set of discretised equations can be written in matrix form as $SX = F$ where S is a matrix containing the elements general stiffness written as

$$S = \begin{bmatrix} S_{pp} & S_{pT} \\ S_{Tp} & S_{TT} \end{bmatrix} \tag{17}$$

and F is a vector containing the loadings written as

$$F = \begin{cases} M_{p_m,p_m} p_m^t - C_{p_m,T_m} T_m^t + Q_{p_m} dt \\ M_{p_f,p_f} p_f^t - C_{p_f,T_f} T_f^t + Q_{p_f} dt \\ M_{T_m,T_m} T_m^t - C_{T_m,p_m} p_m^t + Q_{T_m} dt \\ M_{T_f,T_f} T_f^t - C_{T_f,p_f} p_f^t + Q_{T_f} dt \end{cases} \tag{18}$$

The components in the stiffness matrix S depends on the main unknown variables. Therefore a Picard interation procedure is used to obtain an acceptable solution defined by a determined tolerance. For the current iteration $s+1$ in the current time step $n+1$ the solution dependent coefficient matrix in the

stiffness matrix S are updated by using the weighted average solution vector $X_{n+1}^{s+\theta}$ can be defined as

$$X_{n+1}^{s+\theta} = (1-\theta)X_{n+1}^{s-1} + \theta X_{n+1}^{s} \tag{19}$$

where X_{n+1}^{s-1} and X_{n+1}^{s} are the solution vectors from the two recent iterations in the current timestep $n+1$ and $\theta = \frac{2}{3}$ is the weighing coefficient. For the first iteration $s = 1$, the previous timestep solution is used as

$$X_{n+1}^{0} = X_{n+1}^{1} = X_n \tag{20}$$

where X_n is the solution vector from the previous timestep n. The iterations are repeated until consecutive normalised values of X_{n+1}^{s} agree to within a specified tolerance denoted by ϵ. This tolerance can be written as

$$\frac{||X_{n+1}^{s+1} - X_{n+1}^{2}||}{||X_{n+1}^{s+1}||} \leq \epsilon \tag{21}$$

In this study the tolerance for the solver is chosen to $\epsilon = 0.01$.

3 Model Validation

To ensure that that the simulator produces trustworthy results, a series of validation tests has been performed. The results from the model has been compared to known analytical and numerical solutions. In total three validation tests are performed.

3.1 Validation Test 1 - TH Model

First a coupled Thermal-Hydraulic (TH) model is validated. This is done by comparing the results produced by the simulator to the analytical solution obtained by Bodvarsson (1969) [12]. The model considers a 1D flow through a fracture of dimensions 100 x 100 meters, from an injection well to a production well. The simulation domain for this model is 500 x 100 x 1000 meters. A visual representation of the simulation domain is shown on figure 4.

The analytical solution used to solve the problem was derived by Carslaw and Jaeger in 1959. The solution expresses the temperature of the produced water as a function of x which is the distance from the injection point parallel to the fracture plane. y is the distance into the formation, so perpendicular to the fracture and t which is the time in seconds from the injection was started. This approach assumes that the formation surrounding the fracture is impermeable, so there is no leak-off of fluid into the formation. This means that y can be assumes 0 in equation 22.

$$T(x, y, t) = A \cdot erfc\left(\frac{\alpha x + y}{2\sqrt{at}}\right) + T_s \tag{22}$$

where A is defined as $A = T_{inj} - T_s$, α is a dimensionless parameter given given by $\frac{2\lambda_s}{c_f q}$, where q is the mass flow rate, denoted by the injection rate multiplied by the density of the injected fluid. $q = Q\rho_f$, a is then the thermal diffusivity of the formation surrounding the fracture given by $\frac{\lambda_s}{\rho_s C_s}$

The simulation domain used to solve the problem is shown on figure 4. The simulation is done for four different matrix permeabilities. First an impermeable case is run to match the analytical solution by Bodvarsson (1969) [12]. Then three different cases with increasing permeabilities are done to introduce the effect of leak-off from the fracture.

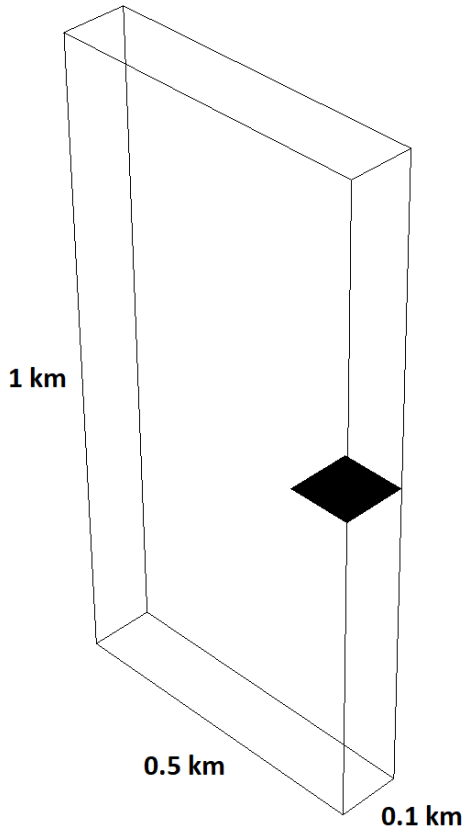

Figure 4: Simulation domain for the numerical solution.

Table 1 shows the different permeability's used in the four different cases.

Table 1: Permeability's used for the four different cases.

	Case 1	Case 2	Case 3	Case 4	Unit
Permeability k_m	10^{-18}	10^{-12}	10^{-11}	10^{-10}	$[m^2]$

The reason $k_m = 10^{-18}\ m^2$ is used for the impermeable case, and not 0 is becouse the simulator can't handle a $k_m = 0$ Therefore a very small permeability is used. $k_m = 10^{-18}\ m^2$ is equvialent to 0.001 mDa which is so small that it can be neglected. Table 2 shows the values used by the simulator for the numerical solution.

Table 2: Values used for analytical and numerical solutions.

Parameter	Value	Unit
Formation		
Density	2820	$\frac{kg}{m^3}$
Porosity	0.01	-
Temperature	100	$°C$
Heat Capacity	1170	$\frac{J}{kg \cdot K}$
Biot Coefficient	1	-
Poisson's Ration	0.25	-
Young's Modulus	$20 \cdot 10^9$	Pa
Heat Conductivity	2.88	$\frac{W}{m \cdot K}$
Thermal Expansion	$2.5 \cdot 10^{-5}$	$°C^{-1}$
Fluid		
Density	1000	$\frac{kg}{m^3}$
Viscosity	1	cP
Heat Capacity	4200	$\frac{J}{kg \cdot K}$
Compressibility	$5 \cdot 10^{-10}$	Pa^{-1}
Heat Conductivity	0.6	$\frac{W}{m \cdot K}$
Thermal Expansion	$7.66 \cdot 10^{-4}$	$°C^{-1}$
Injection Temperature	20	$°C$
Other		
Well Radius	0.05	m
Fracture Aperture	0.001	m
Injection Flow Rate	0.01	$\frac{m^3}{s}$
Production Pressure	0	Pa
With of the Fracture	100	m
Distance Between Wells	100	m

The results of the analytical and the numerical solutions are shown in Figure 5 where the production temperature is plotted as a function of the time that has passed since the injection of cold water was started.

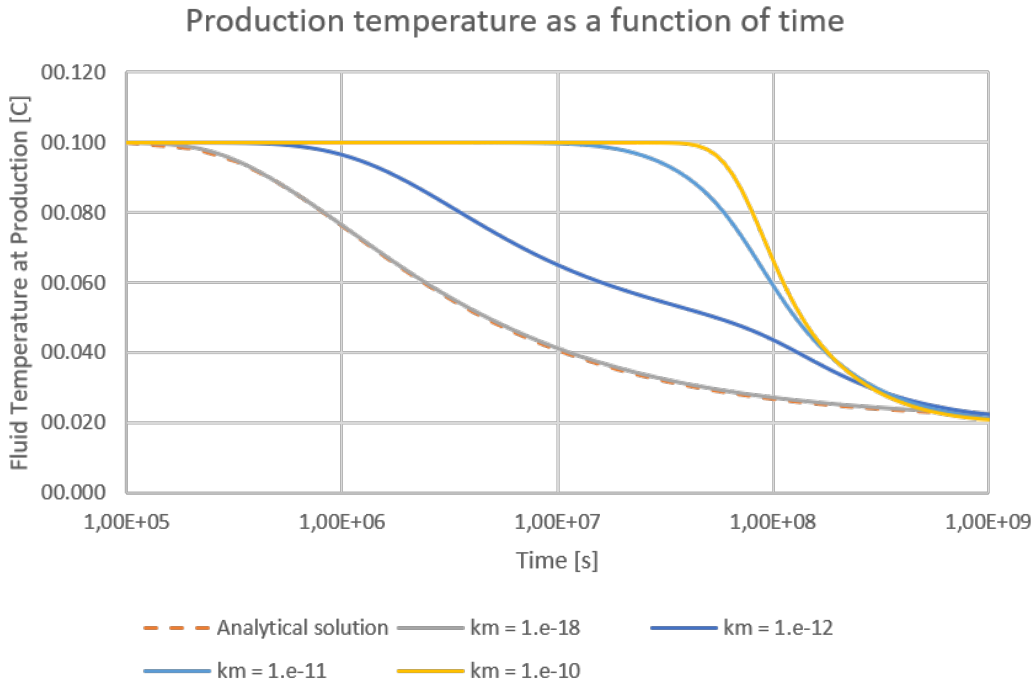

Figure 5: Results for analytical and numerical solutions.

From Figure 5 a very good agreement is found between the analytical solution and the model for the case with no leak-off to or from the formation. On simulations 2 to 4 the effect of leak-off can be seen for increasing permeabilities for the formation.

3.2 Validation Test 2 - TH Model

The second validation test is also a coupled TH model. In this case the propagation of the injected fluid in a infinite fracture is evaluated. An Injection well is placed in the center of a simulation domain measuring 3000 x 3000 x 3000 meters with a fracture in the middle. The temperature of the fluid is evaluated as a function of time and radial distance from the injection well. The results are compared to the analytical solution by [19]

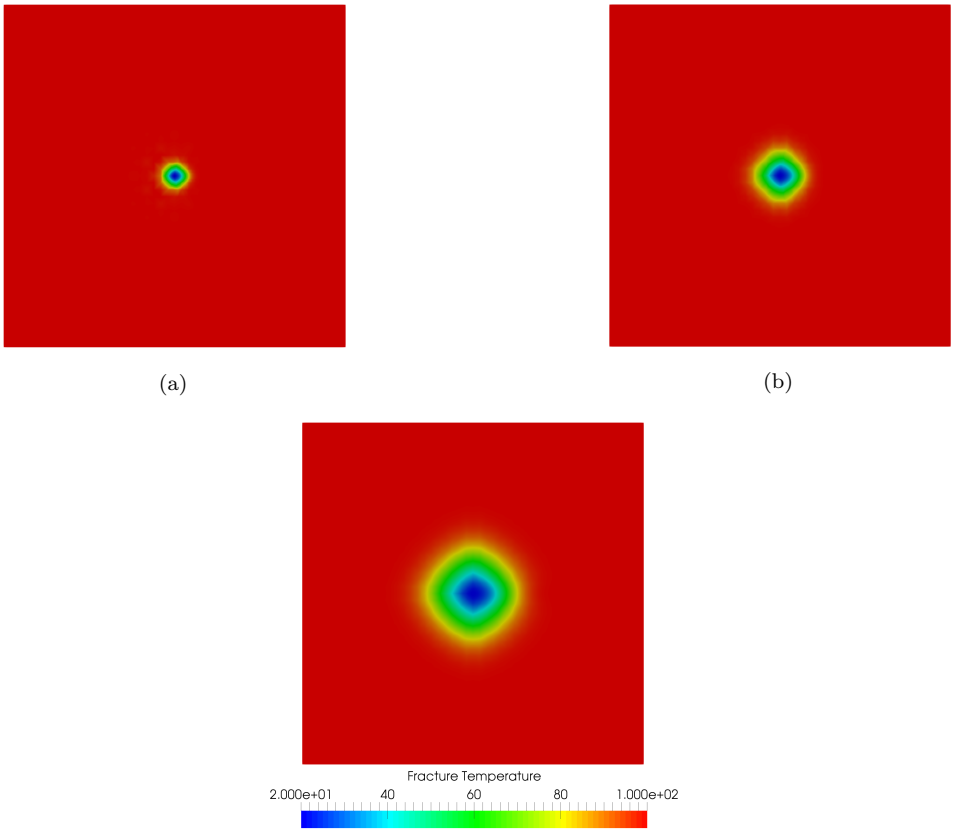

Figure 6: Shows the temperature distribution in the fracture. (a) At $t = 1.e7$ seconds. (b) At $t = 1.e8$ seconds. (c) At $t = 1.e9$ seconds.

The analytical solution to the problem presented by [19] expresses the temperature of the fluid in a infinite fracture as a function of three variables.

$$T_d(r, z, t) = erfc\left[\left(\frac{\pi K_r r^2}{Q\rho_w c_w} + \frac{z}{2}\right)\sqrt{\frac{\rho_r c_r}{K_r t}}\right] \tag{23}$$

The radial distance from the injection point r, the distance orthogonal to the fracture z and the time elapsed since the injection of water begun t.
To reduce the number of variable in the expression some assumption is made. The first assumption is that the rock matrix is assumed impermeable with a permeability of $k_m = 10^{-18}$. This means that leak-off of fluid into the formation can be neglected, so z can be set to zero. The second assumption is that the time t is treated as a constant. This leaves only the the radial distance r as a variable. Three time-steps are considered $t = 10^7$, $t = 10^8$ and $t = 10^9$ seconds. The results of the analytical solution can be seen on figure 7 together with the numerical solution.

A numerical solution to the problem is also found using a coupled thermal hydraulic simulator. A 3D simulation domain is modelled with a size of 3000 x 3000 x 3000 meters. A fracture is placed in the center of the domain, extending the entire length and width of the domain. An injection well is placed in the center and and is injection cold water at a constant rate. Table 3 lists the values used in the simulation.

Table 3: Values used for analytical and numerical solutions.

Parameter	Value	Unit
Formation		
Density	2700	$\frac{kg}{m^3}$
Porosity	0.001	-
Permeability	10^{-18}	m^2
Temperature	100	$°C$
Thermal Expansion	$2.4 \cdot 10^{-5}$	$°C^{-1}$
Thermal Conductivity	2	$\frac{W}{m \cdot K}$
Specific Heat Capacity	1000	$\frac{J}{kg \cdot K}$
Fluid		
Density	1000	$\frac{kg}{m^3}$
Viscosity	1	cP
Compressibility	$5 \cdot 10^{-10}$	Pa^{-1}
Thermal Expansion	$7.66 \cdot 10^{-4}$	$°C$
Specific Heat Capacity	4200	$\frac{J}{kg \cdot K}$
Other		
Injection Flow Rate	0.01	$\frac{m^3}{s}$
Injection Temperature	20	$°C$

The normalized temperature T_d is plotted for both the analytical and the numerical solution in figure 7

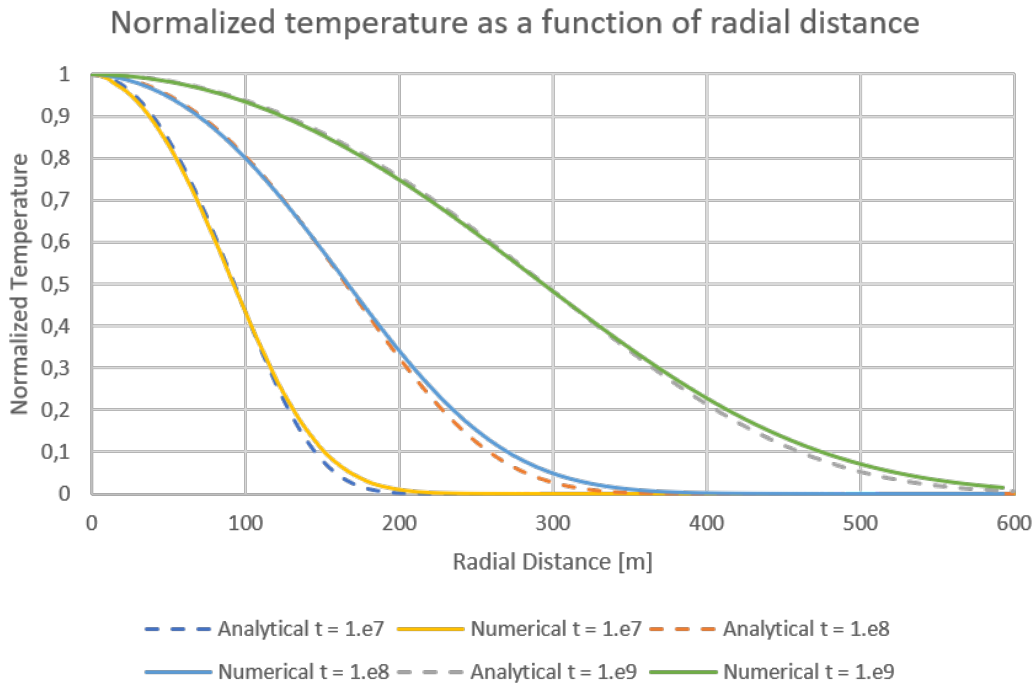

Figure 7: Results for analytical and numerical solutions.

From figure 7 a good agreement between the results obtained by the analytical and the numerical solutions is shown.

3.3 Validation Test 3 - THM Model

The third validation test is a fully coupled THM model. The addition of the mechanics means that the fracture can no longer be assumed rigid, but aperture will change with time as a function of the effective stress. To find the aperture at each step the Barton-Bandi's model is used,

$$a_f = a_0 - \frac{a\sigma_n'}{1 + b\sigma_n'}$$

where a_f is the fracture aperture at a given time, σ_n' is the effective stress, a_0 is the maximum possible aperture when the effective stress is at it's minimum, a_0 is given as 0.0012m and a and b is two constants, determined by two reference states for the effective stress, where the aperture is known. The first known state is $\sigma_n' = 30MPa$ yielding an aperture of $a_f = 2.4 \cdot 10^{-4}m$, and the second known state is $\sigma_n' = 5MPa$ yielding an aperture of $a_f = 7.2 \cdot 10^{-4}m$. With this the constants a and b is found to be $1.6 \cdot 10^{-10}$ and $1.3 \cdot 10^{-7}$.

The simulation domain is a square cube measuring 3000 x 3000 x 3000 meters. In the center a penny shaped fracture with a radius of 500 meters is placed. This fracture is intersected with an injection and a production well 500 meters apart. Figure 8 shows the simulation domain, together with the location of the fracture.

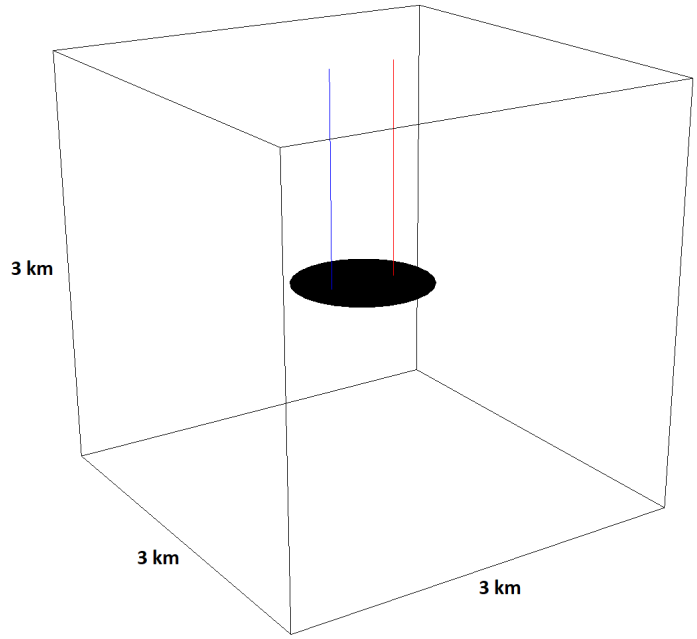

Figure 8: Simulation domain used in the model. The blue and red line indicates the injection and production well, respectivly. They are placed 500 meters apart, and both intersect the penny shaped fracture in the center of the simulation domain. The rarius of the fracture is 500 meters.

Parameters used in the simulation can be seen in table 4.

Using this model, the aperture of the fracture for the 30-year time period is shown on Figure 9.

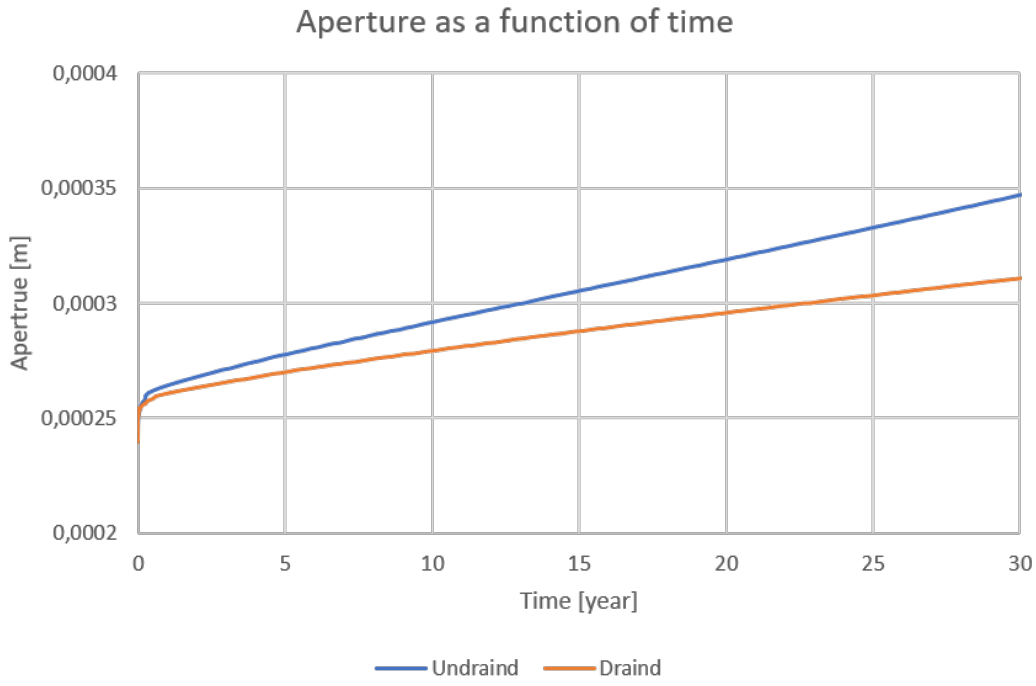

Figure 9: Delevopment of fracture aperture over 30 years.

In contrast to the two previous models, here the mechanics is included in the simulation. Also, the density of the water is no longer assumed constant, but as a function of the pressure and temperature. The density for the fluid is given by equation 24.

$$\rho_f = \rho_r e^{[\beta_f(p_f - p_r) - \alpha_f(T_f - T_r)]} \tag{24}$$

where ρ_r, p_r and T_r are the reference conditions, listed in Table 4. β_f and α_f are respectively the compressibility and the thermal expansion of the fluid, values are listed in Table 3.

Table 4: Values used in the simulation.

Parameter	Value	Unit
Formation		
Density	2500	$\frac{kg}{m^3}$
Porosity	0.01	-
Permeability	10^{-18}	m^2
Temperature		$°C$
Thermal Conductivity	3.5	$\frac{W}{m \cdot K}$
Specific Heat Capacity	790	$\frac{J}{kg \cdot K}$
Thermal Expansion (Drained)	$24 \cdot 10^{-6}$	$°C^{-1}$
Thermal Expansion (Undrained)	$30 \cdot 10^{-6}$	$°C^{-1}$
Fluid		
Viscosity	$0.142 \cdot 10^{-3}$	$Pa \cdot s$
Compressibility	$5.11 \cdot 10^{-10}$	Pa^{-1}
Reference Pressure	$34 \cdot 10^6$	Pa
Thermal Expansion	$7.66 \cdot 10^{-4}$	$°C$
Specific Heat Capacity	4460	$\frac{J}{kg \cdot K}$
Reference Temperature	200	$°C$
Other		
Injection Flow Rate	0.0125	$\frac{m^3}{s}$
Production Pressure	$34 \cdot 10^6$	Pa
Injection Temperature	50	$°C$

Figure 10 shows the results of both the drained and the undrained conditions, together with the results by Guo et al (2016) [22].

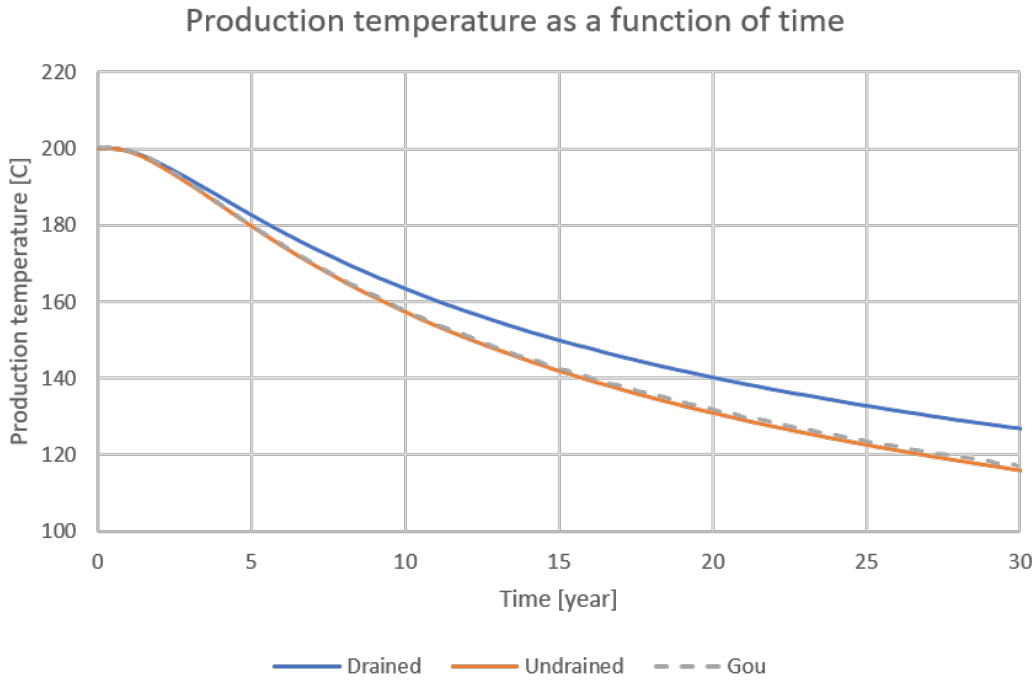

Figure 10: Delevopment of fracture aperture over 30 years.

A very good agreement is shown between the simulation for the undrained case and the results by Guo et al (2016) [22]. With these results the validation of the mechanics is successful.

4 Results

In this section the results for a single fracture simulation domain, a homogeneous fracture distribution with three different levels of fracture density and connectivity, a heterogeneous fracture distribution also with three different levels of fracture density and connectivity and a case with long fractures only in one direction in the reservoir, in this case only two fracture cases are investigated. One case where the long fractures aren't connected with each other, and one case where the long fractures are connected by smaller fractures going in the opposite direction. For the two cases with homogeneous and heterogeneous the low fracture cases is shown here, the two renaming cases for the medium and higher fracture cases are shown in appendixes A, B and C, respectively.
The results for production temperature profiles, well pressure profiles and energy production for the cases are investigated. All cases are investigated with both a (TH) model and a (THM) model to see the effect of the mechanics when using RJD in a geothermal reservoir.

4.1 Single Fracture Model

Three models were used to simulate a doublet well system in a domain with only a single fracture, a (H), (TH) and a (THM) model. Three fracture apertures were tested with each of the models. For each model, and each fracture aperture two cases were investigated. One where four laterals of 50 meters where added to the well, in this case the laterals didn't connect the wells to the fracture. And one where the length of the laterals was increased to 100 meters, in this case the laterals did connect the wells to the fracture. Figure 11 shows the simulation domain with both 50 and 100 meter laterals. In this section the results of the simulations on the cases with a high fracture aperture is shown. The other results are shown in appendix A.

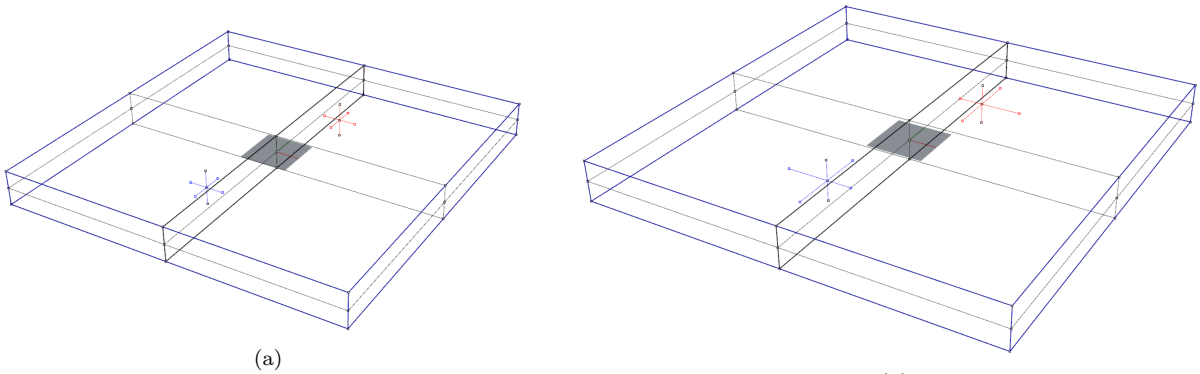

(a) (b)

Figure 11: Simulation domain for the single fracture case. (a) The wells with four 50 meter laterals added, here the laterals are not connected to the fracture. (b) The wells with four 100 meter laterals added, here the laterals connect to the fracture.

The dimensions of the simulation domain are 1000x1000x100 meters, the fracture is placed in the center of the domain and extend the full height and length of the simulation domain. The wells are placed on opposite sides of the fracture with equal distance to the fracture, the distance between the well is 500 meters. Parameters used in the simulations are listed in table 5.

Table 5: Parameters used for single fracture simulations.

General Parameters			
Parameter	Symbol	Value	Unit
Matrix Porosity	ϕ	0.25	-
Matrix Permeability	k_m	10^{-14}	m^2
Injection flow rate	Q_{inj}	0.1	$\frac{m^3}{s}$
Production flow rate	Q_{prod}	0.1	$\frac{m^3}{s}$
(H) model			
Parameter	Symbol	Value	Unit
Fluid Viscosity	μ_f	10^{-3}	$Pa \cdot s$
(TH) model			
Parameter	Symbol	Value	Unit
Fluid Viscosity	μ_f	Temperature Dependant	$Pa \cdot s$
Initial Rock Matrix Temperature	T_0	80	^oC
Injection Temperature	T_{inj}	20	^oC
Matrix Heat Capacity	C_m	790	$\frac{kg \cdot m^2}{K \cdot s^2}$
Fluid Heat Capacity	C_f	4200	$\frac{kg \cdot m^2}{K \cdot s^2}$
Matrix Thermal Conductivity	λ_m	3.5	$\frac{W}{m \cdot K}$
Fluid Thermal Conductivity	λ_f	0.6	$\frac{W}{m \cdot K}$
(THM) model			
Parameter	Symbol	Value	Unit
Fluid Viscosity	μ_f	Temperature Dependant	$Pa \cdot s$
Initial Rock Matrix Temperature	T_0	80	^oC
Injection Temperature	T_{inj}	20	^oC
Matrix Heat Capacity	C_m	790	$\frac{kg \cdot m^2}{K \cdot s^2}$
Fluid Heat Capacity	C_f	4200	$\frac{kg \cdot m^2}{K \cdot s^2}$
Matrix Thermal Conductivity	λ_m	3.5	$\frac{W}{m \cdot K}$
Fluid Thermal Conductivity	λ_f	0.6	$\frac{W}{m \cdot K}$
Young's Modulus	E	50	GPa
Poisson's Ratios	ν	0.25	-
Biot Coefficient	α	1	-

For the (THM) model the Barton-Bandis model Bandis et al., 1983; Barton et al., 1985 [10, 11] is used to evaluate the fracture aperture equation 1. The two reference states used to determine the model parameters a and b are a_{f1} is the initial aperture, $\sigma_{n1} = 40MPa$ and a_{f2} is the initial aperture times three, $\sigma_{n2} = 25MPA$. This yields the following values for the model parameters a and b shown in table 6.

Table 6: Model parameters for the Barton-Bandis model.

Initial Fracture Aperture [m]	a	b
$4.93 \cdot 10^{-4}$	$1.7748 \cdot 10^{-9}$	$4 \cdot 10^{-7}$
$9.86 \cdot 10^{-5}$	$3.5496 \cdot 10^{-10}$	$4 \cdot 10^{-7}$
$4.93 \cdot 10^{-5}$	$1.7748 \cdot 10^{-10}$	$4 \cdot 10^{-7}$

4.1.1 (H) model

When only the flow in the model is considered, the pressure needed to sustain the flow rates specified in table 5 becomes constant when the flow reaches a steady state flow, as is shown on figure 12.

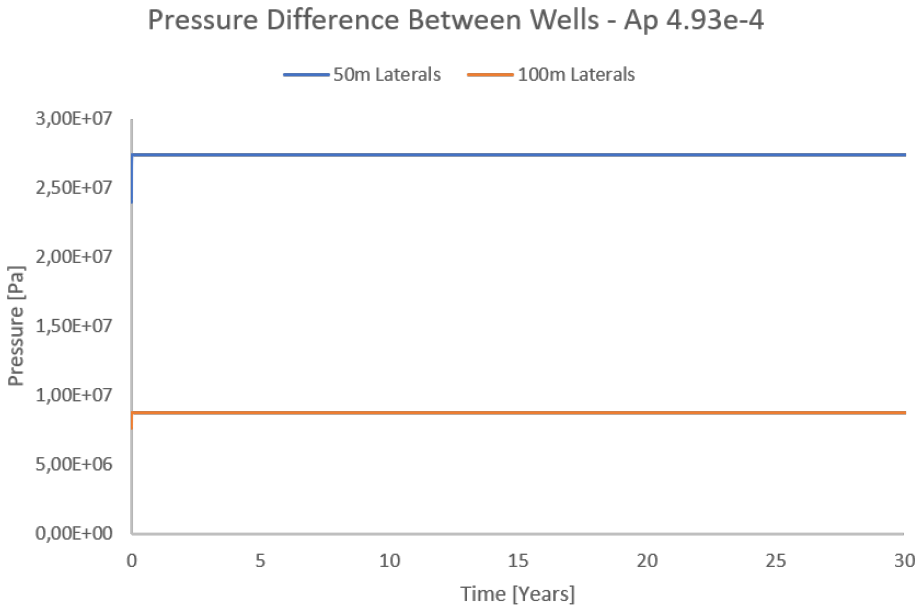

Figure 12: Pressure difference between the wells for the $a_f = 4.93 \cdot 10^{-4}\ m$ case with both 50 and 100 meter laterals.

From figure 12 it is seen that steady state is reached almost immediately after injection is started, and from that point the pressures stays constant. This is because all the effects that would influence the pressures are ignored in this simulation. It is clear to see from figure 12 that connecting the wells using RJD to drill small lateral micro-holes significantly decreases the pressure difference needed for the given flow. Similar simulations have been performed on the same domain with different fracture apertures. They show the same trends steady state is reached almost immediately after injection is started and the pressure stays constant from that point. These results is shown in appendix A1 on figure 36.

4.1.2 (TH) model

Now the temperature is included in the simulations, the pressure difference between the well can no longer be considered constant due to the thermal effects included in the simulations. The pressures difference is shown on figure 13.

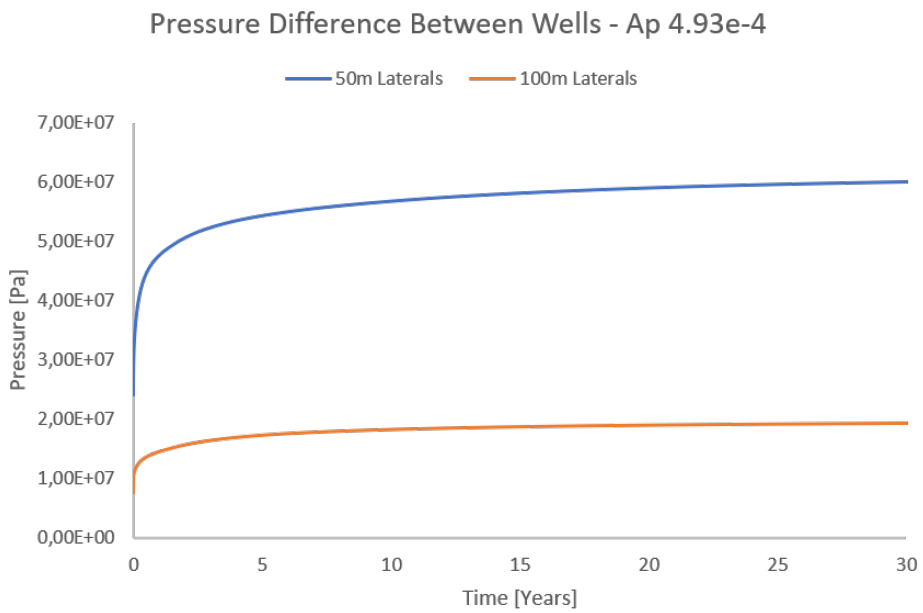

Figure 13: Pressure difference between the wells for the $a_f = 4.93 \cdot 10^{-4}$ m case with both 50 and 100 meter laterals.

Comparing the results with those from the (H) model shown on figure 12 it is seen that the (TH) model is slower in reaching the a steady state, and even after steady state is reached the pressure difference is still slowly increasing over the entire simulation period. Again, it is shown that being able to connect the wells to an excising fracture significantly decreases the pressure difference needed. Results for cases with lower apertures is shown in appendix A2 on figure 37. The same trend for the pressure is shown here, although the difference between the two cases is lower due to the lower fracture aperture.

The temperature profile is also now considered. Figure 14 shows the production temperature profile over the simulation period.

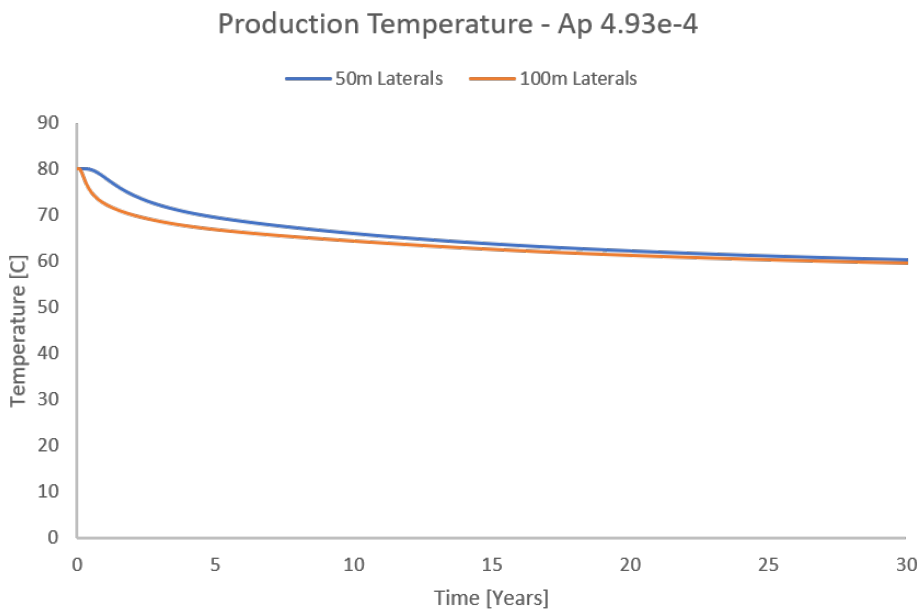

Figure 14: Production temperature profile for the $a_f = 4.93 \cdot 10^{-4}$ m case with both 50 and 100 meter laterals.

It is clear to see that the thermal breakthrough happens a short time after injection is started. The early separation between the cases with 50 and 100-meter laterals happens because the case with 100-meter laterals the wells is almost directly connected through the laterals and the fracture. Whereas the case with 50-meter laterals is not connected, therefore the fluid has to flow though the matrix also. Similar simulations for cases with a lower fracture aperture can be seen on figure 38 in appendix A2. Here there is no separation in the early production state, this is because the fracture aperture is becoming very small, therefore the flow becomes more and more matrix dominated. Whereas the case shown on figure 14 the flow is fracture dominated.

4.1.3 (THM) model

Finally, a (THM) model has been used on the single fracture case. Here the fracture aperture is no longer constant, this has an impact on the results. Figure 15.

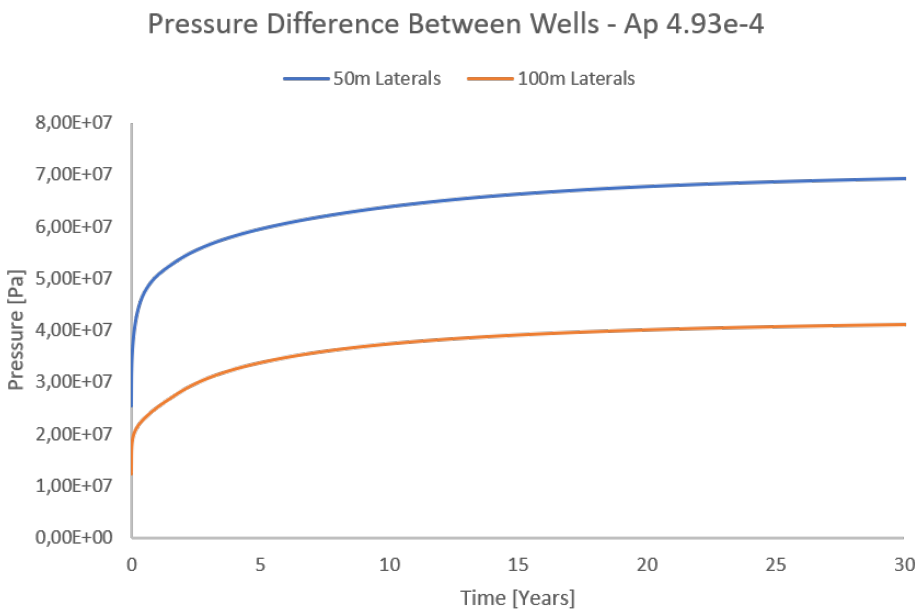

Figure 15: Pressure difference between the wells for the $a_f = 4.93 \cdot 10^{-4}$ m case with both 50 and 100 meter laterals.

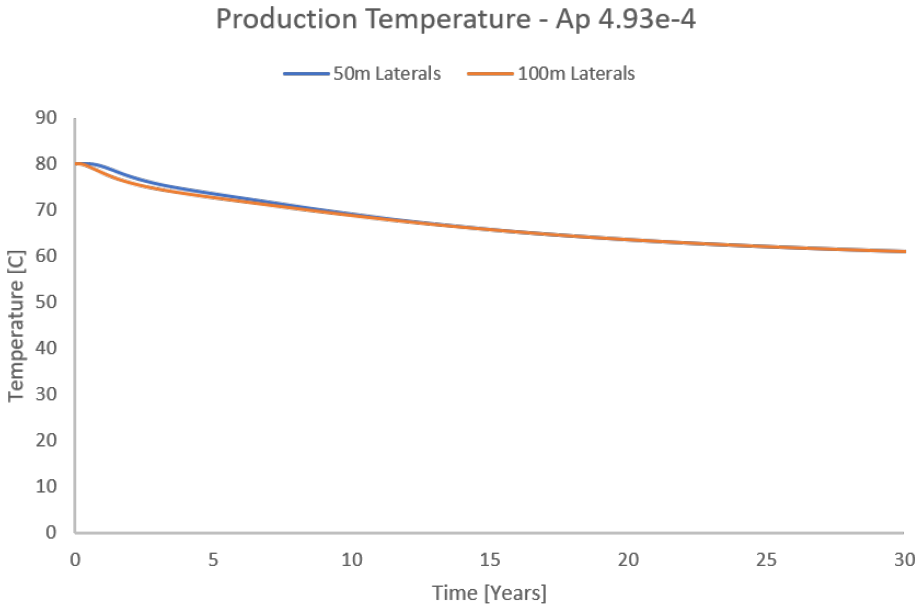

Figure 16: Production temperature profile for the $a_f = 4.93 \cdot 10^{-4}$ m case with both 50 and 100 meter laterals.

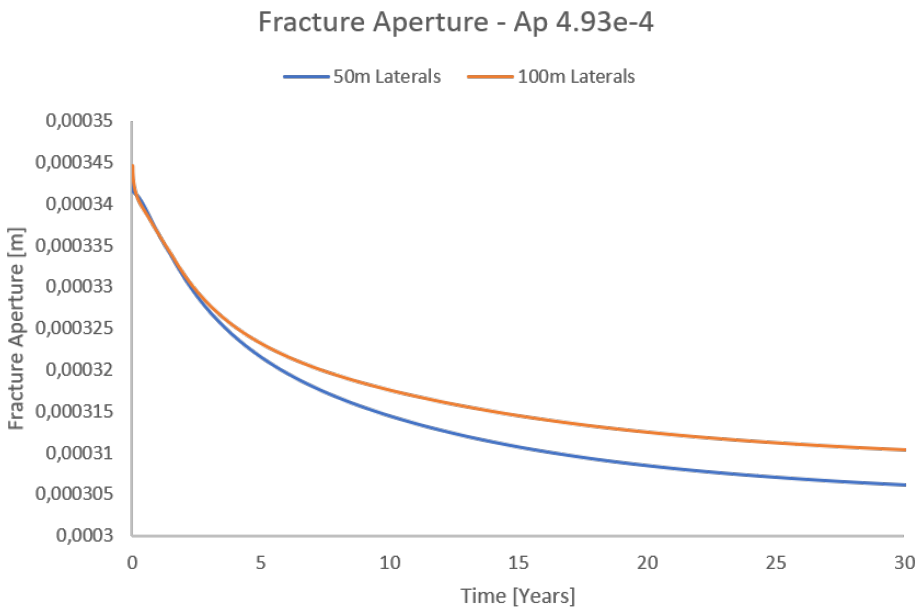

Figure 17: Average fracture aperture for the $a_f = 4.93 \cdot 10^{-4}$ m case with both 50 and 100 meter laterals.

When using a fully coupled (THM) solver compared to a (TH) solver the notable difference is on the pressure difference between the injection well and the production well. The thermal drawdown after 30 years of production does not significantly change, this is seen by comparing the thermal drawdown profiles on figures 14 and 17 for a (TH) solver and a (THM) solver, respectively. The difference is seen in the first part of the production period mainly for the case with 100-meter laterals, the separation period between the case with 50-meter laterals and 100-meter laterals is longer in the (TH) case. This is because the fracture aperture in the (TH) case is constant throughout the entire production period. Whereas the fracture aperture in the (THM) case is reducing over the production period, as shown of figure 17. This reduction of the fracture aperture restricts the fluid flow through the fracture, and thereby delaying the thermal break through time.

This reduction in the fracture aperture also influence the necessary pressure difference between the injection well and production well to keep a constant flow rate through the reservoir. This is also duo to the fact that a smaller fracture aperture results in a more restricted flow, therefore in order to keep a constant flow rate the pressure difference has to be increased. This effect is dictated by Darcy's low eq. 25 where a smaller fracture aperture equals a smaller effective permeability k_{eff}. So, in order to keep Q constant ΔP has to increase. On figure 17 it is seen that the fracture aperture is higher for the case with 100 meter laterals than for the case with 50 meter laterals. This is duo to the fact that in the case with 100-meter laterals the wells are directly connected to the fracture, whereas the case with 50-meter laterals the wells are not directly connected with the fracture. This means that the fracture in the case with 100-meter laterals are exposed to the cold injection fluid faster than the 50-meter lateral case. This means that the cooling of the formation will assist in keeping the fracture open, duo to contraction of the rock when cooled down by the injection fluid.

When comparing the pressure difference between the injection well and the production well for the (TH) and (THM) solver on figure 13 and 15, respectively. Here it is clear to see the effect of the mechanics

in the (THM) solver. The overall trend where the case with 100-meter lateral requires a lower pressure difference then the case with 50-meter laterals is still the same. But the pressure difference needed in the (THM) case is higher than that of the (TH) case, especially for the 100-meter lateral case a significant increase is seen. This indicates that using a (TH) solver will underestimate the pressures needed to keep a constant flow rate compared to a (THM) solver.

Similar simulations have also here been performed on the same simulation domain only with lower initial fracture apertures. In these cases, the results for varying lateral length track better with each other. This is the effect of the lower initial fracture aperture, the flow in the domain is more matrix dominant compared to the case shown on figures 15, 16 and 17. The results can be seen in appendix A3 on figures 39, 40 and 41.

4.2 1D Permeability Analysis

To obtain a better understanding of the different fracture sets a 1D permeability test is performed on each one, in both the x and y direction. This is done by closing all but two opposite boundaries, and applying a pressure difference from one boundary to the other, thereby creating a flow through the reservoir. The pressure difference ΔP is chosen to *1 MPa*. Then Darcy's equation 25 is used to calculate the effective permeability k_{eff} of the reservoir using the flow Q from the simulation outputs.

$$Q = \frac{k_{eff}}{\mu_f} \frac{A\Delta P}{L} \tag{25}$$

Where μ_f is the viscosity of the fluid, A is the cross-section area in the direction of the flow and L is the distance from one boundary to the other. The permeability of the matrix is set to be $k_m = 10^{-17} m^2$. To ensure that the simulation reach a steady state flow the simulation time was 300 years (94.608e8 seconds).

4.2.1 Results For Fracture Set With Homogeneous Fracture Distribution

The results of the 1D permeability tests of the homogeneous fracture sets shown on figure 18. in x and y direction is shown in table 7 and 8, respectively.

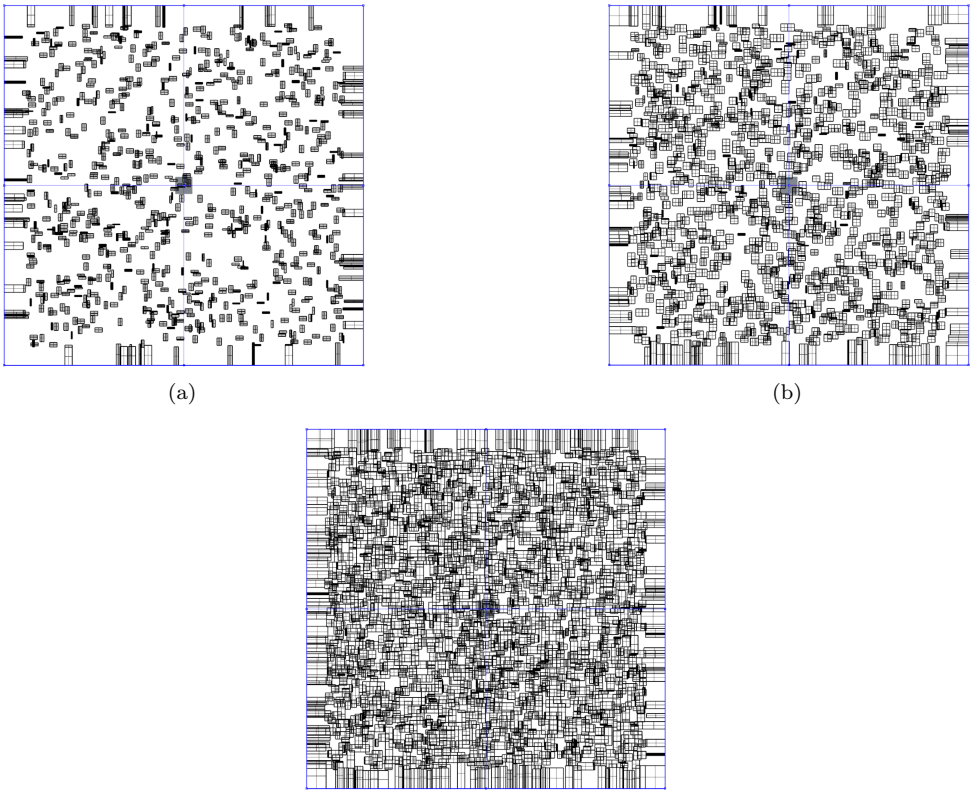

(a) (b)

(c)

Figure 18: Fracture set with a homogeneous fracture distribution for different fracture densities. (a) Low fracture density and connectivity. (b) Medium fracture density and connectivity. (c) High fracture density and connectivity.

Table 7: 1D permeability test in the x-direction, for the homogeneous fracture set.

(TH) Model		
	Effective permeability $[m^2]$	
Fracture aperture $[m]$	2e-4	1e-3
Low fracture density and connectivity	3.3999e-17	3.4102e-17
Medium fracture density and connectivity	1.3213e-16	1.4055e-16
High fracture density and connectivity	6.1969e-15	7.5045e-13
(THM) Model		
	Effective permeability $[m^2]$	
Fracture aperture $[m]$	2e-4	1e-3
Low fracture density and connectivity	3.40958e-17	3.4096e-17
Medium fracture density and connectivity	1.3997e-16	1.3997e-16
High fracture density and connectivity	9.4091e-14	9.4091e-14

Table 8: 1D permeability test in the y-direction, for the homogeneous fracture set.

(TH) Model		
	Effective permeability $[m^2]$	
Fracture aperture $[m]$	2e-4	1e-3
Low fracture density and connectivity	2.6942e-17	2.7177e-17
Medium fracture density and connectivity	1.0816e-16	1.1228e-16
High fracture density and connectivity	6.5237e-15	7.9112e-13
(THM) Model		
	Effective permeability $[m^2]$	
Fracture aperture $[m]$	2e-4	1e-3
Low fracture density and connectivity	2.7160e-17	2.7160e-17
Medium fracture density and connectivity	1.1777e-16	1.1777e-16
High fracture density and connectivity	9.9275e-14	9.9160e-14

From the results shown in table 7 and 8 it is shown that the fractures in the reservoir doesn't support a dominant flow direction in the reservoir. When using the fully coupled THM model the initial aperture of the fractures has no effect on the effective permeability when steady state flow is reached. Steady state flow isn't reached before the fracture aperture also is at equilibrium with the reservoir conditions, and therefore not changing any more. Figure 19 and 20 shows the matrix pressure of the reservoir when steady state flow is reached with initial fracture aperture of 1 millimeter for the TH and THM model, respectively.

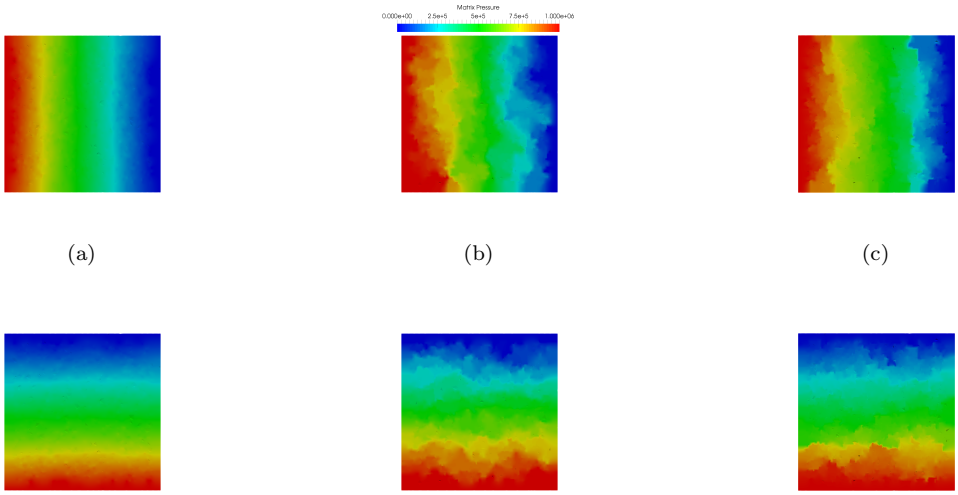

(a) (b) (c)

(d) (e) (f)

Figure 19: Matrix pressure in the reservoir when steady state flow conditions is reached using a TH model. On the top row the flow is in the x direction, and on the bottom row the flow is in the y direction. (a, d) Low fracture density. (b, e) Medium fracture density. (c, f) High fracture density.

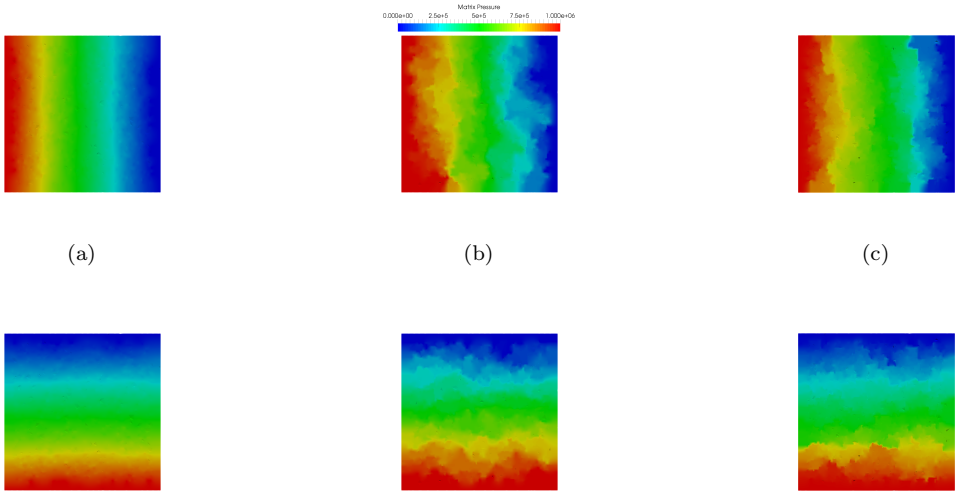

(a) (b) (c)

(d) (e) (f)

Figure 20: Matrix pressure in the reservoir when steady state flow conditions is reached using a THM model. On the top row the flow is in the x direction, and on the bottom row the flow is in the y direction. (a, d) Low fracture density. (b, e) Medium fracture density. (c, f) High fracture density.

Figures 19 and 20 support the results in table 7 and 8 that the fractures doesn't support a dominant flow direction in the reservoir. This is as to be expected since the fractures are homogeneously distributed in the reservoir. Matrix pressure in the reservoir with an initial fracture aperture of 0.2 millimeter is shown in appendix B1.

4.2.2 Results For Fracture Set With Heterogeneous Fracture Distribution

A 1D permeability test has also been performed for the fracture case with heterogeneous fracture distribution shown on figure 21. The results of the test in both the x and y direction is shown in table 9 and 10, respectively.

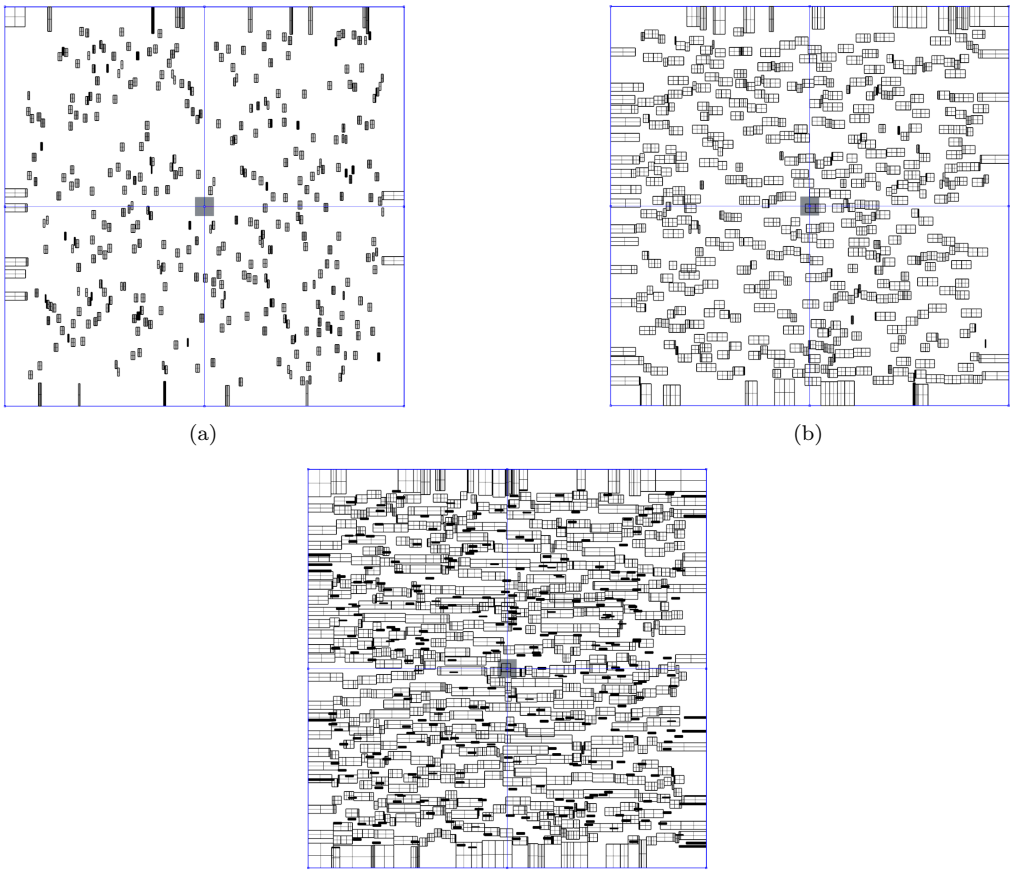

Figure 21: Fracture set with a heterogeneous fracture distribution for different fracture densities. (a) Low fracture density and connectivity. (b) Medium fracture density and connectivity. (c) High fracture density and connectivity.

Table 9: 1D permeability test in the x-direction, for the heterogeneous fracture set.

(TH) Model		
	Effective permeability $[m^2]$	
Fracture aperture $[m]$	2e-4	1e-3
Low fracture density and connectivity	2.291e-17	2.2920e-17
Medium fracture density and connectivity	8.6524e-17	8.7746e-17
High fracture density and connectivity	5.0134e-16	5.7847e-16
(THM) Model		
	Effective permeability $[m^2]$	
Fracture aperture $[m]$	2e-4	1e-3
Low fracture density and connectivity	2.29195e-17	2.2920e-17
Medium fracture density and connectivity	8.7677e-17	8.7677e-17
High fracture density and connectivity	5.7280e-16	5.7280e-16

Table 10: 1D permeability test in the y-direction, for the heterogeneous fracture set.

(TH) Model		
	Effective permeability $[m^2]$	
Fracture aperture $[m]$	2e-4	1e-3
Low fracture density and connectivity	2.4711e-17	2.4783e-17
Medium fracture density and connectivity	3.7272e-17	3.7483e-17
High fracture density and connectivity	6.1037e-17	6.2823e-17
(THM) Model		
	Effective permeability $[m^2]$	
Fracture aperture $[m]$	2e-4	1e-3
Low fracture density and connectivity	2.4779e-17	2.4779e-17
Medium fracture density and connectivity	3.7471e-17	3.7471e-17
High fracture density and connectivity	6.2708e-17	6.2708Ee-17

The results shown in table 9 and 10 indicates that the case with low fracture density doesn't have a dominant flow direction, whereas the cases with medium and high fracture densities shows a dominant flow direction. In both cases the dominant flow direction is in the x direction.
The matrix pressure in the reservoir after 300 years when the flow has reached a steady state is shown on figure 22 and fig: Hetro-Frac Pressure THM model when using a TH and THM model, respectively. The initial fracture aperture is here 1 millimeter. Results for the cases with initial fracture aperture 0.2 millimeter is shown in appendix B2.

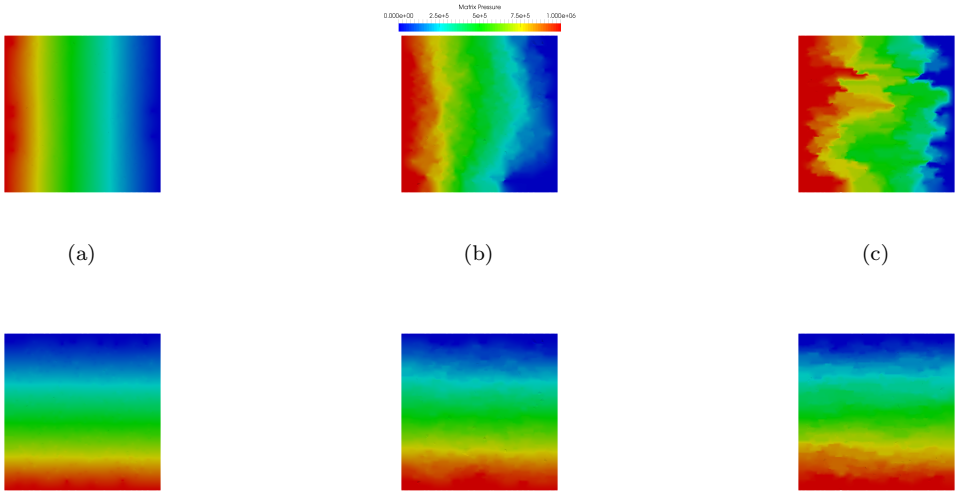

(a) (b) (c)

(d) (e) (f)

Figure 22: Matrix pressure in the reservoir when steady state flow conditions is reached using a TH model. On the top row the flow is in the x direction, and on the bottom row the flow is in the y direction. (a, d) Low fracture density. (b, e) Medium fracture density. (c, f) High fracture density.

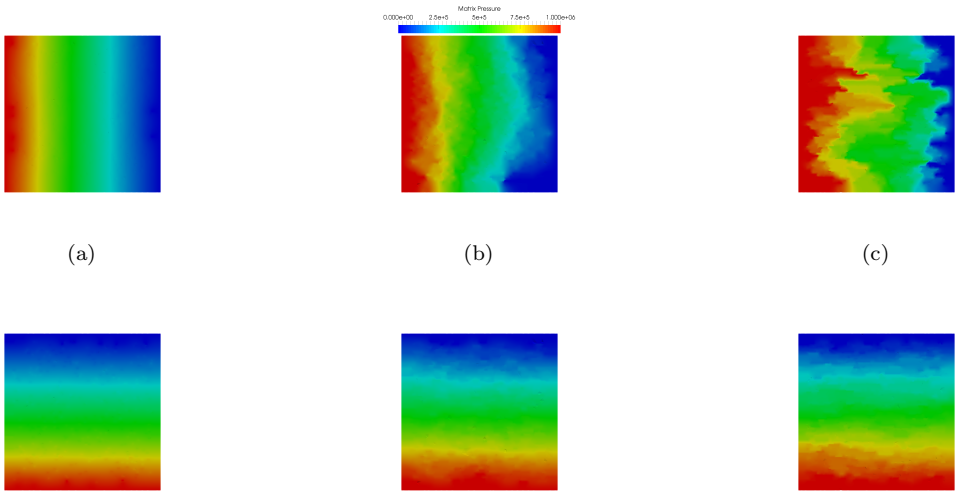

(a) (b) (c)

(d) (e) (f)

Figure 23: Matrix pressure in the reservoir when steady state flow conditions is reached using a THM model. On the top row the flow is in the x direction, and on the bottom row the flow is in the y direction. (a, d) Low fracture density. (b, e) Medium fracture density. (c, f) High fracture density.

From figure 22 and 23 it can be seen that especially the case with high fracture density has a dominant flow direction, as indicated by the results in table 9 and 10 in the x direction. The results also shows that the medium fracture case has a dominant flow direction in the x direction, this however is not that clear to see on figures 22 and 23.

4.2.3 Results For Fracture Set With Long Heterogeneous Fracture Distribution

The last fracture set contains longer fractures with a heterogeneous distribution, as shown on figure 24. In this case only two sets are investigated, compared to the three cases in the previous cases. The results of the 1D permeability test are shown in tables 11 and 12 for the x and y direction, respectively.

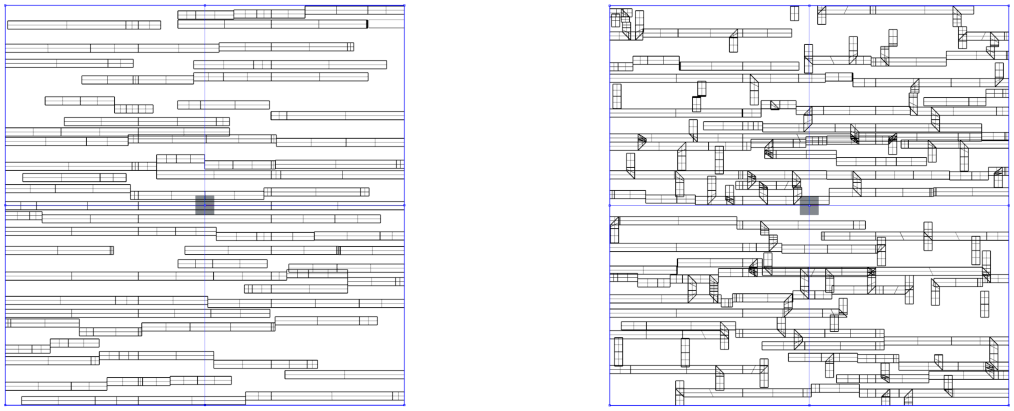

(a) (b)

Figure 24: Fracture set with long fractures. (a) Long non-connected fracture. (b) Long connected fractures.

Table 11: 1D permeability test in the x-direction, for the fracture set.

(TH) Model		
	Effective permeability $[m^2]$	
Fracture aperture $[m]$	2e-4	1e-3
Low fracture density and connectivity	6.05479e-15	4.8123e-13
High fracture density and connectivity	5.2962e-15	5.7646e-13
(THM) Model		
	Effective permeability $[m^2]$	
Fracture aperture $[m]$	2e-4	1e-3
Low fracture density and connectivity	6.30372e-14	6.3037e-14
High fracture density and connectivity	7.3012e-14	7.3012e-14

Table 12: 1D permeability test in the y-direction, for the fracture set.

(TH) Model		
	Effective permeability $[m^2]$	
Fracture aperture $[m]$	2e-4	1e-3
Low fracture density and connectivity	4.5053e-17	4.7983e-17
High fracture density and connectivity	1.2227e-16	1.6815e-16
(THM) Model		
	Effective permeability $[m^2]$	
Fracture aperture $[m]$	2e-4	1e-3
Low fracture density and connectivity	4.7732e-17	4.7732e-17
High fracture density and connectivity	1.6320e-16	1.6320e-16

From the results in table 11 and 12 it is clear to see that the fractures create a dominant flow direction in the x direction compared to the y direction. This is also clear when looking at the matrix pressure in the reservoir, shown on figures 25 and 26. Below is shown the pressure distribution for an initial fracture aperture of 1 mm. in appendix B3 the pressure distribution for an initial fracture aperture of 0.2 millimeter.

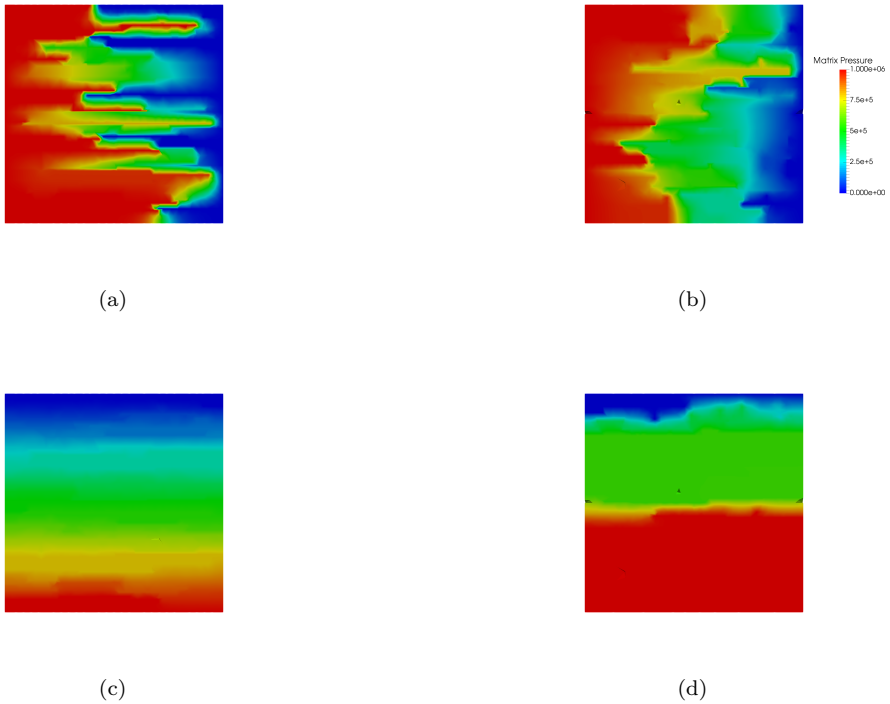

(a) (b)

(c) (d)

Figure 25: Matrix pressure in the reservoir when steady state flow conditions is reached using a TH model. On the top row the flow is in the x direction, and on the bottom row the flow is in the y direction. (a, c) non connected fracture case. (b, d) Connected fracture case.

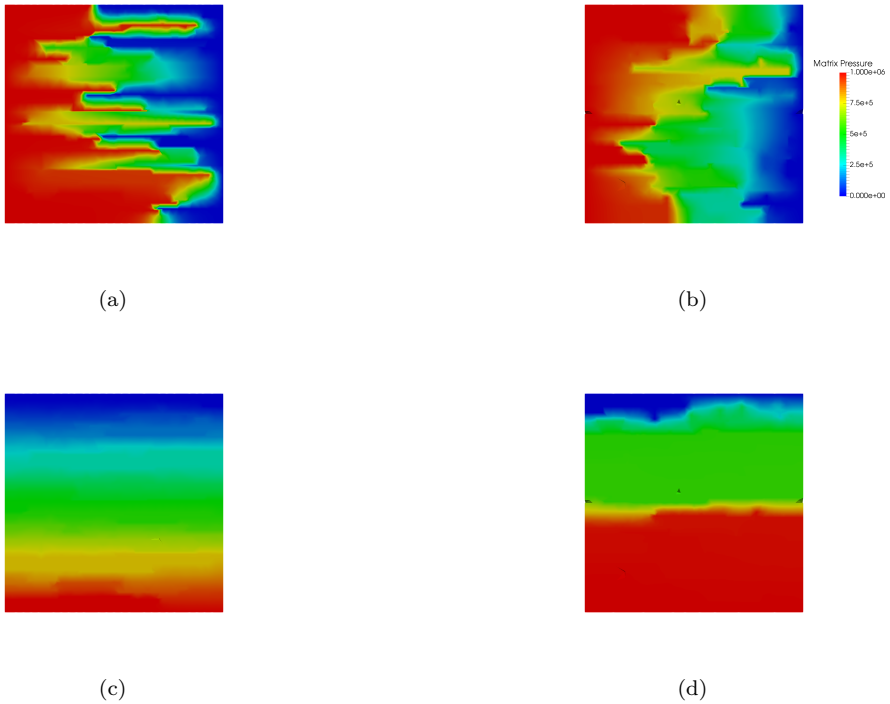

(a) (b)

(c) (d)

Figure 26: Matrix pressure in the reservoir when steady state flow conditions is reached using a THM model. On the top row the flow is in the x direction, and on the bottom row the flow is in the y direction. (a, c) non connected fracture case. (b, d) Connected fracture case.

Another interesting observation about the fracture sets is that for the non-connected fracture case the dominant flow path is in the bottom of the reservoir when looking at figures 25 and 26. Where in the connected case the dominant flow path is in the top of the reservoir when looking at figures 25 and 26. These three fracture cases will be used to study the effect of using RJD to improve the performance of geothermal heat recovery systems.

4.3 Temperature Analysis

In this section the effect of using RJD technology to create small lateral wells to an excising well on the thermal draw down and thermal breakthrough of a geothermal reservoir. Both simulation with a TH model and a THM model has been carried out, on all three fracture sets. The reason for doing this is to see if the use of RJD technology has the potential to delay either the thermal draw down or the thermal breakthrough, or best of all both. These to factors is important in estimating the potential in a geothermal reservoir, since the energy produced from a geothermal reservoir is strongly related to the production temperature. So, if the use of RJD can delay the thermal draw down, thus keeping the production temperature higher for a longer production period.
Here the simulation results for all three fracture distribution cases are shown for the case with low fracture densities, the results for the medium and high fractures densities are shown in appendix C.

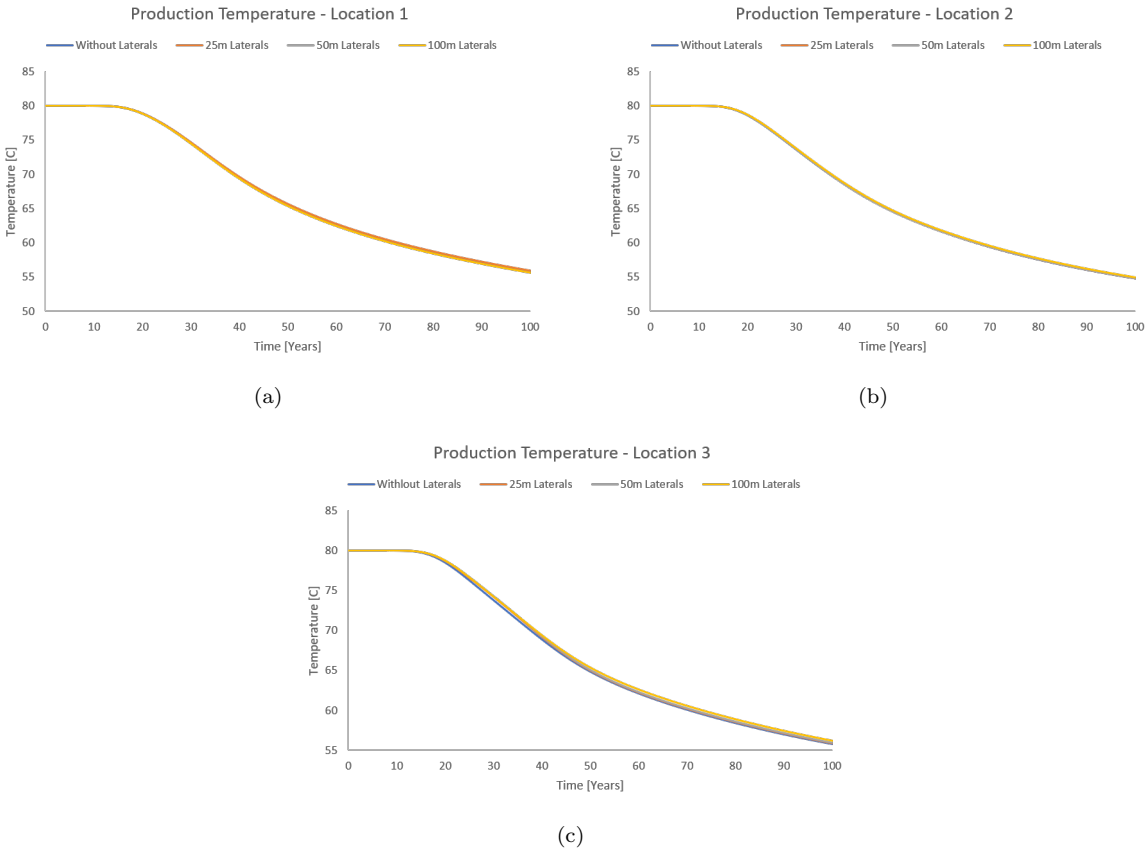

Figure 27: Production temperature profile for the low fracture density fracture set with homogeneous fracture distribution for three well locations. (a) Wells placed in the matrix far away form the fractures in the reservoir. (b) Wells placed closer to the fractures in the reservoir, but not connected. (c) Wells connected to the fractures in the reservoir.

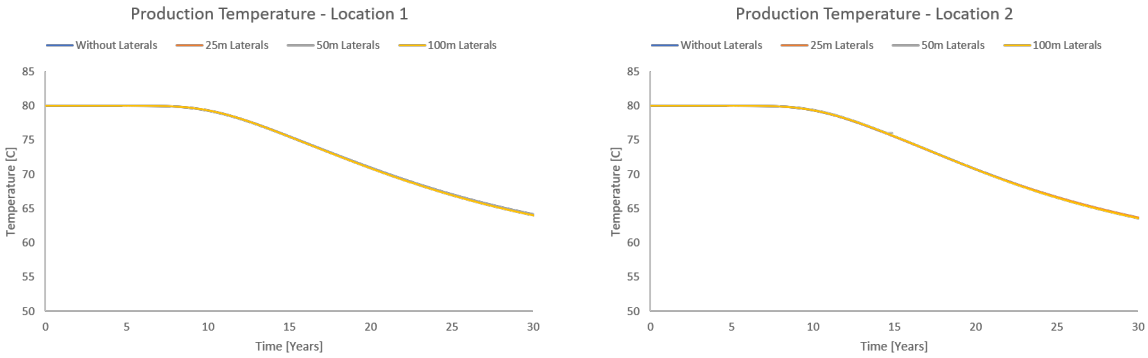

(a)

(b)

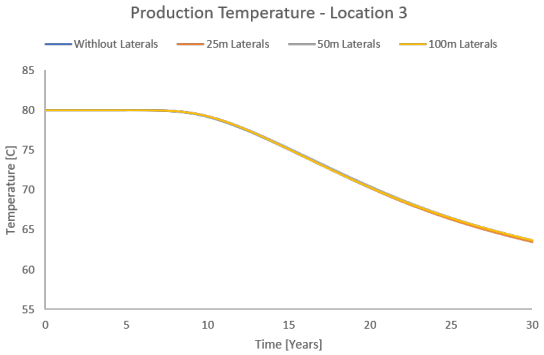

(c)

Figure 28: Production temperature profile for the low fracture density fracture set with heterogeneous fracture distribution for three well locations. (a) Wells placed in the matrix far away form the fractures in the reservoir. (b) Wells placed closer to the fractures in the reservoir, but not connected. (c) Wells connected to the fractures in the reservoir.

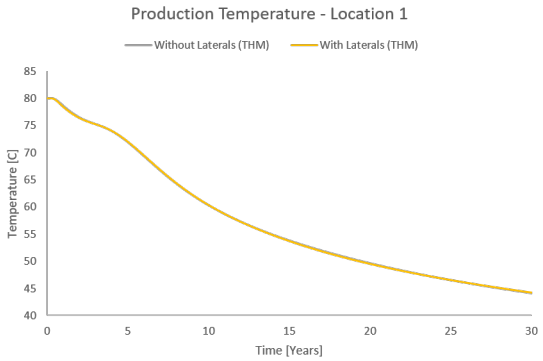

(a)

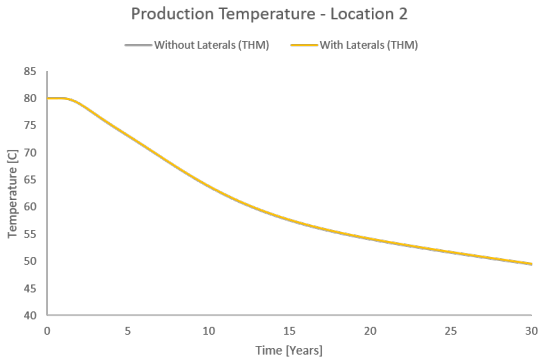

(b)

Figure 29: Production temperature profile for the low fracture density fracture set with long heterogeneous fracture distribution for three well locations. (a) Wells placed in the matrix far away form the fractures in the reservoir. (b) Wells connected to the fractures in the reservoir.

On figures 27, 28 and 29 temperature profiles are shown for the low fracture densities cases for all three fracture sets. From this it is clear that using RJD technology to delay the thermal breakthrough, or slow down the thermal draw down has no effect. This is backed up by similar simulations for the fracture sets

with medium and high fracture densities, as shown in appendix C1, C2 and C3.

4.4 Pressure Analysis

In this section the effect of using RJD to create small lateral wells from a vertical well completion on the down hole pressures needed to sustain a constant flow rate through the geothermal reservoir. The pressure difference between the injection well and the production well is a main parameter in calculating the amount of energy needed by the pumps to sustain the flow. Therefore, if using RJD technology can lower the pressure difference between the injection well and the production well needed to sustain a constant flow rate the overall energy balance of the geothermal reservoir can be improved. As for the temperature analysis simulations on the three fracture sets has been performed both using a TH model and a THM model. The results from the cases with low fracture densities and connectivity's is shown on figures 30, 31 and 32 below. The remaining results for the cases with medium and high fracture densities is shown in appendix D.

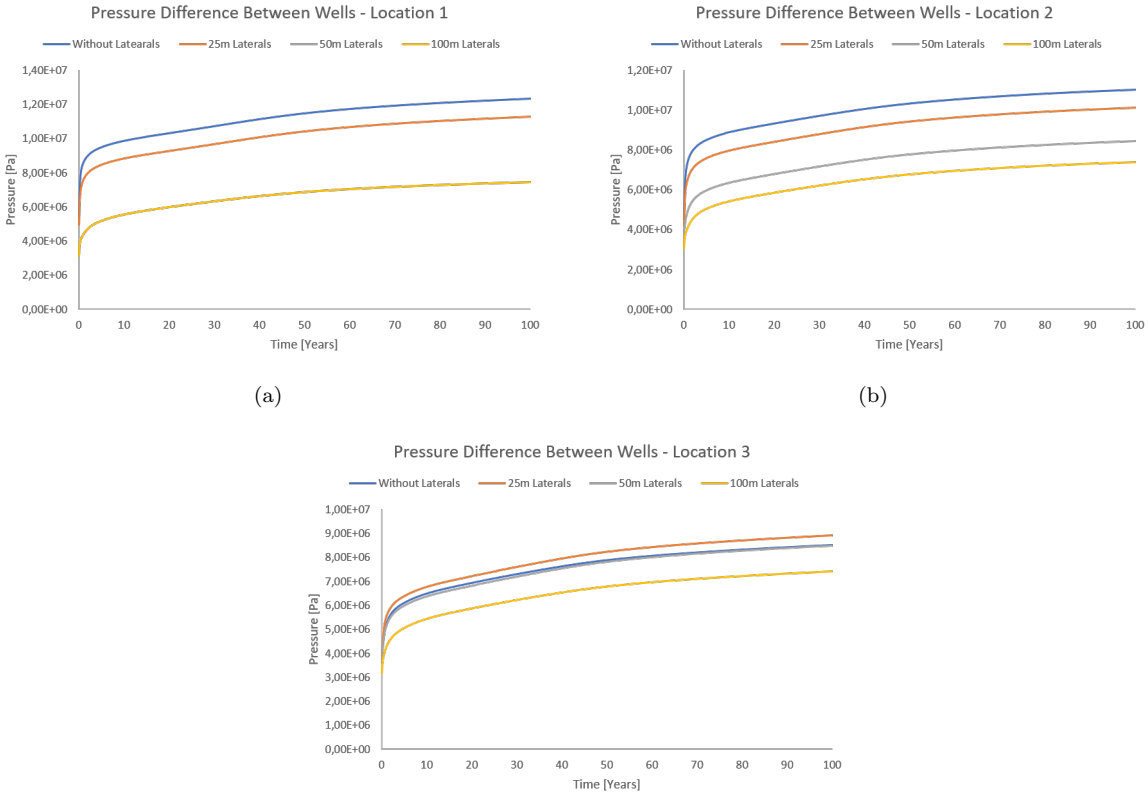

Figure 30: Pressure difference between the injection well and the production well for the low fracture density fracture set with homogeneous fracture distribution for three well locations. (a) Wells placed in the matrix far away form the fractures in the reservoir. (b) Wells placed closer to the fractures in the reserfvoir, but not connected. (c) Wells connected to the fractures in the reservoir.

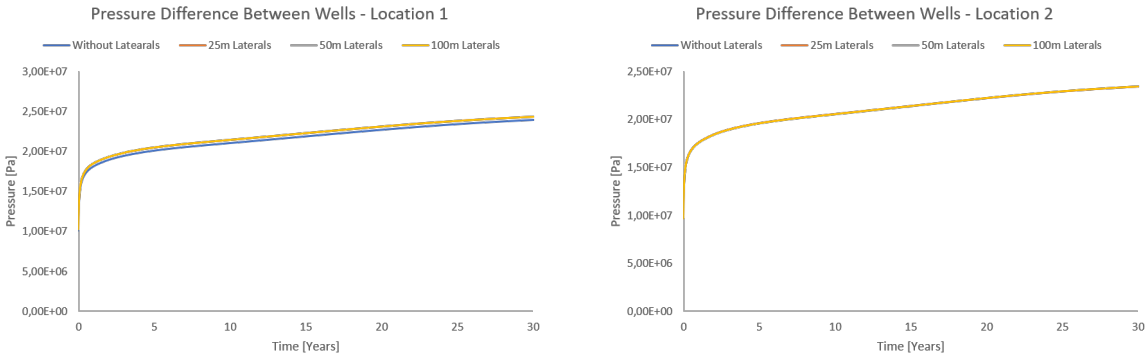

(a)

(b)

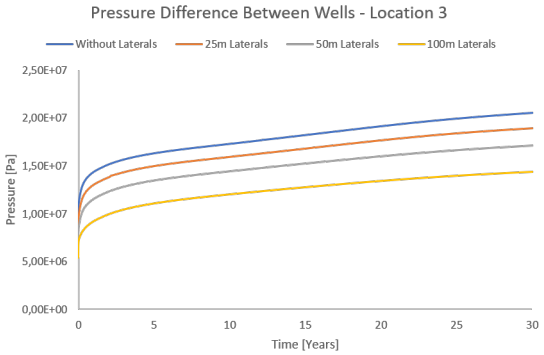

(c)

Figure 31: Pressure difference between the injection well and the production well for the low fracture density fracture set with heterogeneous fracture distribution for three well locations. (a) Wells placed in the matrix far away form the fractures in the reservoir. (b) Wells placed closer to the fractures in the reservoir, but not connected. (c) Wells connected to the fractures in the reservoir.

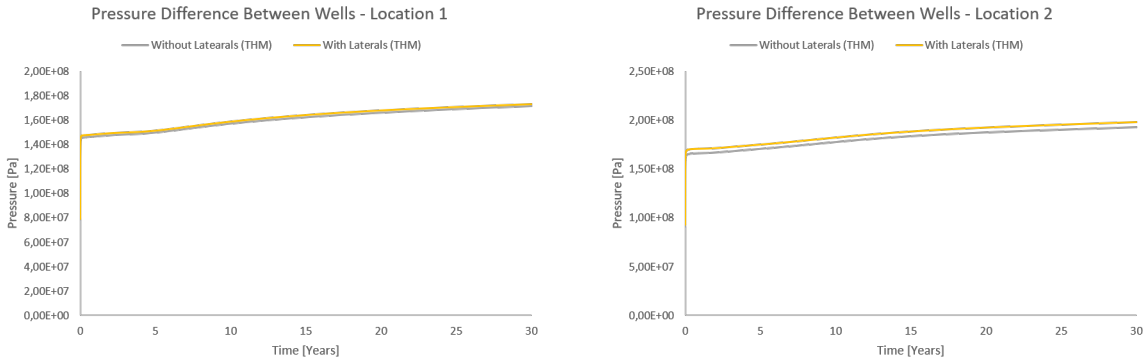

(a)

(b)

Figure 32: Pressure difference between the injection well and the production well for the low fracture density fracture set with long heterogeneous fracture distribution for three well locations. (a) Wells placed in the matrix far away form the fractures in the reservoir. (b) Wells connected to the fractures in the reservoir.

Here the conclusion isn't as clear as in the temperature case. When looking at the pressure difference between the injection well and production well in the fracture sets with homogeneous fracture distribution,

as shown on figure 30 it can be seen that using RJD technology to create lateral micro-holes decreases the needed pressure difference between the wells. The longer the laterals the larger the decrease in the pressure difference, this is also the case for more dense fracture cases with the same homogeneous distribution, as shown in appendix D1. When looking at the fractures with a heterogeneous distribution the effect on the pressure isn't as clear. In this case the well location relative to the fractures is a significant factor in the effect of the laterals. As shown on figure 31 location 1 and 2 isn't suitable for using RJD, whereas location 3 is suitable for using RJD to decrease the pressure difference. Similar simulations for cases with higher densities have been done, and shows the same results. That the well location is a significant factor on the effect of the laterals on the pressure difference. On 32 it is seen that the use of RJD techniques to create lateral micro-holes has no effect on the pressure difference needed to sustain the flow.

4.5 Energy Calculations

With the results found in the previous sections, especially the shown effect of the RJD on the down hole pressures of the wells, the energy reserve of the geothermal reservoirs can be evaluated. The net energy gain from a geothermal reservoir can be expressed by subtracting the energy needed to sustain the down hole pressures needed at both wells from the generated energy off the produced fluid. This is expressed in eruption 26.

$$E_{net} = E_g - E_p \tag{26}$$

Crooijmans et al., (2016) [17] expressed the generated energy from the reservoir as follows

$$E_g = \rho_f c_f Q \int_t^{t_{LT}} (T - LT) dt \tag{27}$$

Where ρ_f is the density of the fluid, c_f is the specific heat capacity of the fluid, Q is the flow rate, T is the production temperature LT is the minimum temperature that the power plant can produce energy at. The energy required by the pump to sustain the down hole pressures was derived by Williems et al., 2017 [29] as follows

$$E_p = \int_0^{t_{LT}} \frac{Q\Delta P}{\epsilon_{pump}} dt \tag{28}$$

Where ΔP is the pressure difference between the injection well and the production well. ϵ_{pump} is an expression for the energy conversion efficiency of the pump used, in this study 0.7 is chosen for ϵ_{pump}. From equation 28 it is clear to see that if ΔP decreases, then the needed energy for the pump also decreases. This will result in an increase in the net energy, provided the generated energy E_g stays the same. Given that the generated energy only has two variables in the expression, the flow rate and the production temperature. The flow rate is kept constant throughout the entire production period, therefore this is no longer a variable, the production temperature is the only variable. The use of RJD is proved to have a negligible effect on the thermal draw down of a geothermal reservoir as shown on figures 27, 28 and 29.

Here energy calculations for a geothermal reservoir with a heterogeneous fracture distribution with a low fracture density is shown. Similar results for geothermal reservoirs with a medium and high fracture density is shown in appendix E. The net energy for the three well location cases is calculated using the results from the (THM) simulations using equations 26, 27 and 28. The results is shown on figure 33.

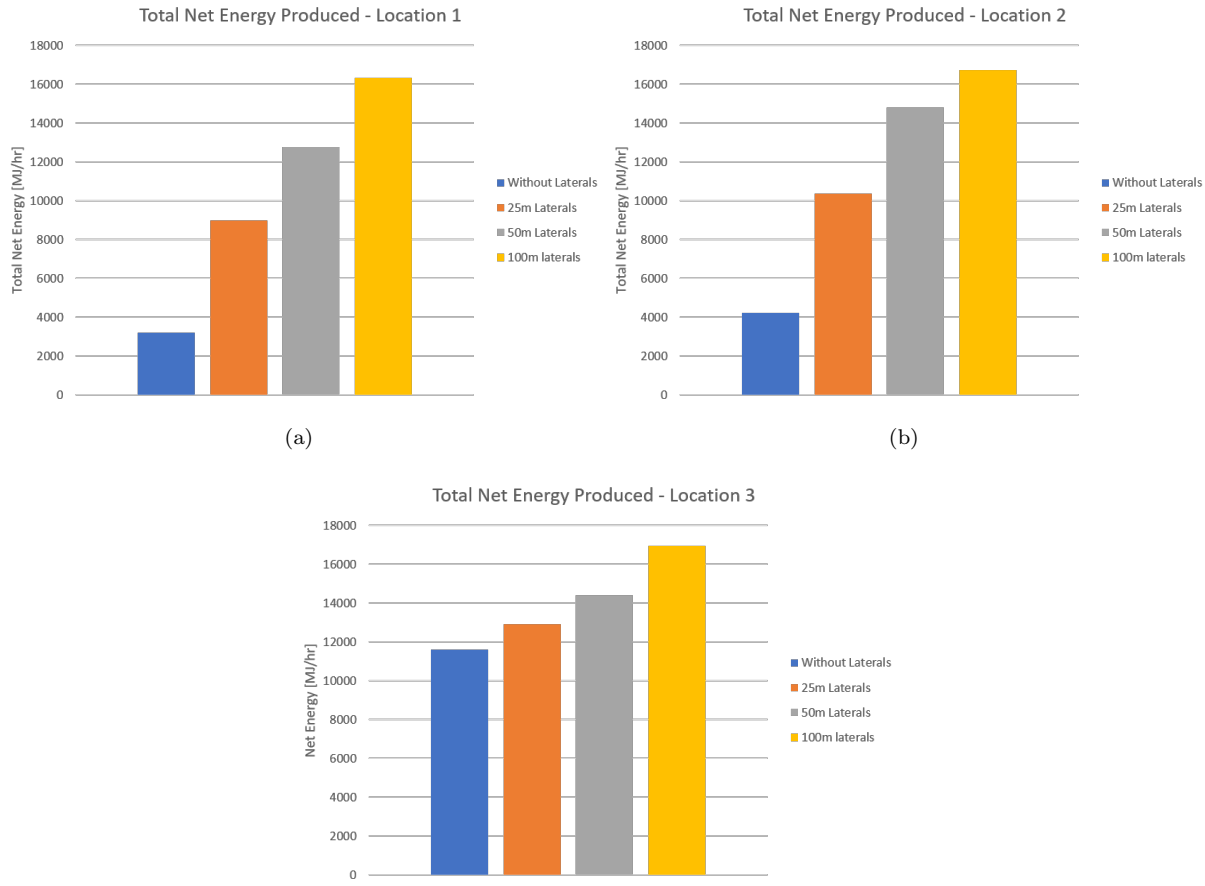

Figure 33: Total amount of net energy for a geothermal reservoir when the reservoir is produced to an abandonment time of $LT = 65°C$. The reservoir has a low fracture permeability and connectivity for different well locations. (a) Well placed in the matrix away from the fracture network. (b) Well placed in the matrix but close to the fracture network. (c) Well placed so the intersect the fracture network.

The minimum production temperature LT is chosen to be $65°C$, and the reservoir is produced to this point. The results shown on figure 33 shows that using RJD has a significant impact on the net energy production of a geothermal reservoir. Looking at the results on figure 33 it is shown that the effect of the RJD in dependent on the well location. As the well location gets closer to the fractures the effect of RJD decreases. The effect of RJD is found to be decreasing with an increasing fracture density and fracture connectivity. This can be seen in appendix E1 on figure 58 and 59, where similar simulations has been performed for geothermal reservoirs with medium and high fracture density and connectivity, respectively.

Using that the CSMP solver simulates several smaller time steps to simulate the entire production period, then equations 27 and 28 can be rewritten to express the the energy as a function of time.

$$E_{g,i} = \rho_f c_f Q(T - LT)\left(\frac{t_{i+1} - t_i}{2} + t_i\right) - \left(\frac{t_i - t_{i-1}}{2} + t_{i-1}\right) \tag{29}$$

and

$$E_{p,i} = \frac{Q\Delta P}{\epsilon_{pump}}\left(\frac{t_{i+1} - t_i}{2} + t_i\right) - \left(\frac{t_i - t_{i-1}}{2} + t_{i-1}\right) \tag{30}$$

where t_i is the time in seconds since production was started to the i^{th} step in the simulation. Equations 29 and 30 is now used instead of equations 27 and 28 to evaluate the energy potential of the geothermal reservoir. The results of this is shown on figure 34 for the same geothermal reservoir as used on figure 33.

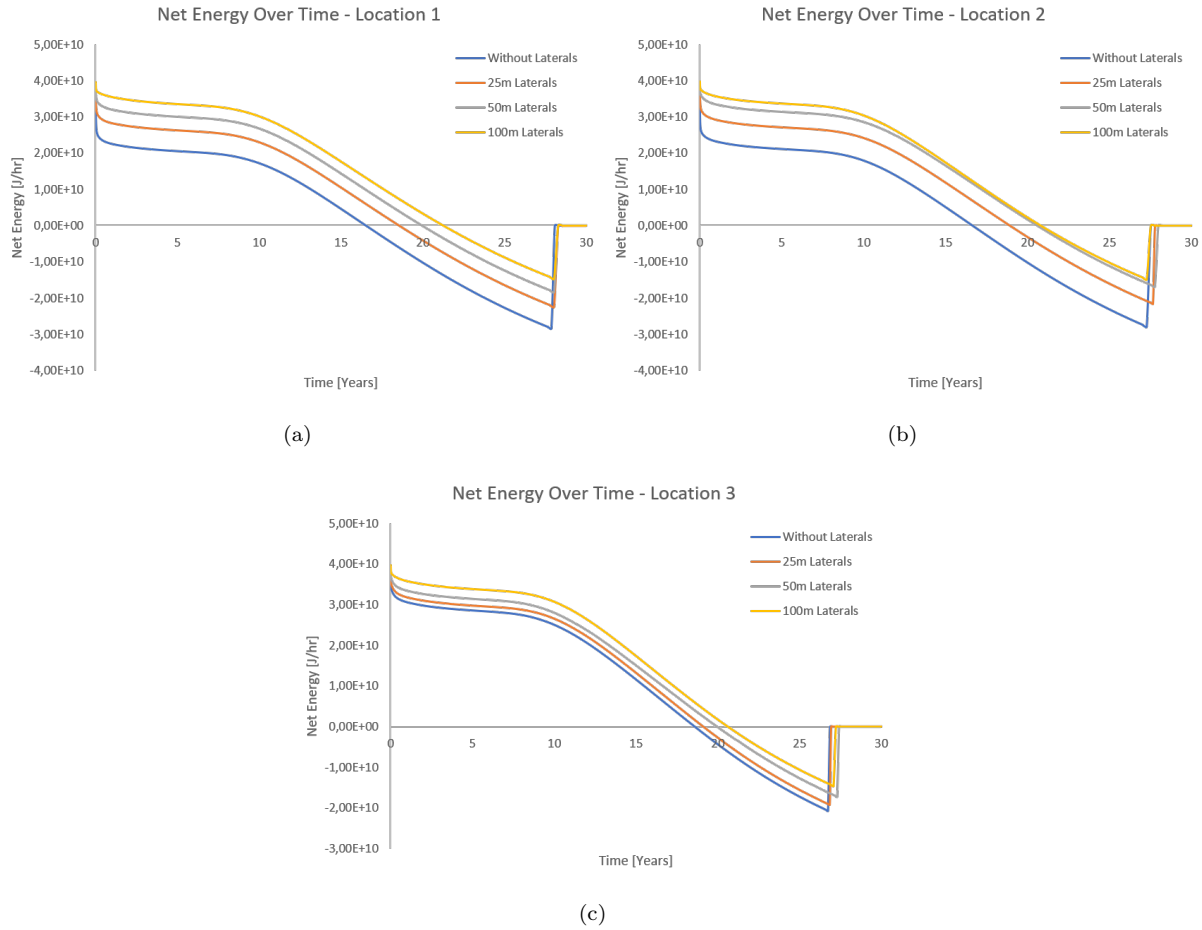

Figure 34: The net energy shown on figure 33 plotted as a function of production time.

This indicate that it is not optimal to produce the reservoir to the $65°C$ that the power plant is capable of. The net energy is shown to be negative in the late part of the production period due to the increasing pressure difference needed to sustain the flow rate, and the lower energy production due to the decreasing production temperature. It is shown that the use of RJD can improves the time of which the reservoir is profitable with multiple years. The same trend with negating relation between used energy to sustain production and the amount of produced energy is shown in appendix E2 for a geothermal reservoir with medium and high fracture densities. Using this information, the optimal abandonment time for the reservoir can be found. The minimum possible production temperature LT is kept at $65°C$ in equation 27 but the production is this time stopped when the net energy becomes zero. So, instead of using t_{LT} as the upper integration limit in equations 27 and 28 $t_{E_{net}=0}$ is used. The total amount of net energy under these conditions is shown in figure 35. Additional simulations have been performed with higher fracture densities, and the results is show in appendix E3.

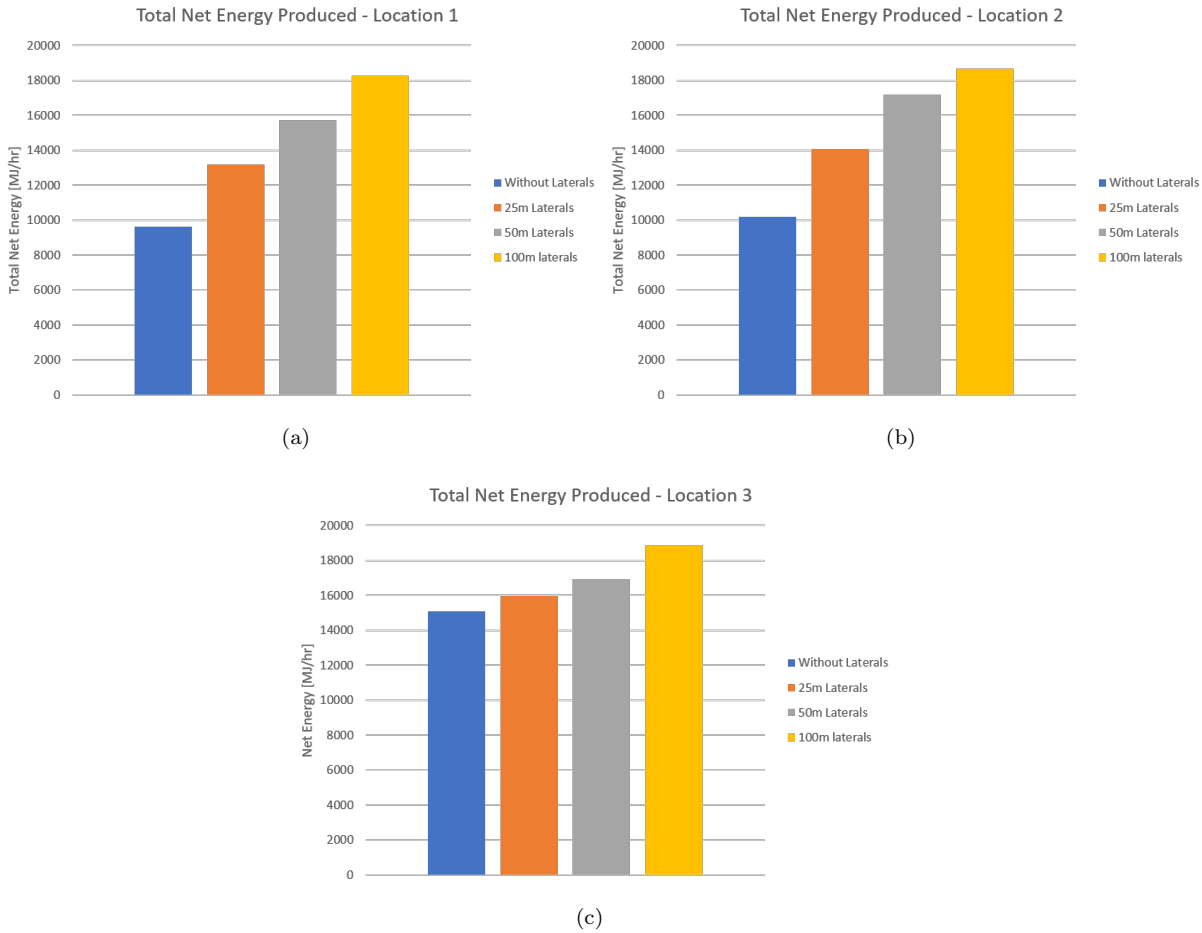

Figure 35: The amount of net energy produced on figure 33 corrected for the optimal abandonment time as found on figure 34.

Comparing the results shown on figure 33 with those shown on figure 35 indicates the importance of finding the optimal abandonment time when evaluating a geothermal reservoir, and the lifetime of such reservoir. The difference between producing to an abandonment temperature of $65°C$, as dictated by the capacity of the power plant. And to end production earlier when the net energy becomes zero is summarized in table 13.

Table 13: Comparison of total net energy for different abandonment times, for a reservoir with low fracture density with different well locations.

Abandonment time	Net Energy $[MJ/hr]$		
	$T_{prod} = 65°C$	$E_{net} = 0$	Difference [%]
Location 1			
Without Laterals	3,220	9,614	198.57
25m Laterals	9,003	13,174	46.33
50m Laterals	12,781	15,712	22.93
100m Laterals	16,336	18,279	11.89
Location 2			
Without Laterals	4,213	10,197	142.04
25m Laterals	10,357	14,061	35.76
50m Laterals	14,785	17,190	16.27
100m Laterals	16,732	18,659	11.52
Location 3			
Without Laterals	11,600	15,074	29.95
25m Laterals	12,915	15,972	23.67
50m Laterals	14,396	16,943	17.69
100m Laterals	16,958	18,876	11.31

This shows that significant improvements can be made to the energy potential of a geothermal reservoir using RJD. These improvements are based on the fact that the use of RJD significant decreases the pressure difference needed to sustain the production rate. The results listed in table 13 is for a reservoir with low fracture density. The largest improvement is for the case where RJD isn't used. This is because the net energy for this case becomes negative first, whereas the case where RJD is used to create 100-meter laterals has the smallest improvement because the net energy becomes negative last. This is shown on figure 34.

5 Conclusion

A fully coupled Thermal-Hydro (TH) and Thermal-Hydro-Mechanical (THM) numerical model based on the Finite Element Method (FEM) is used to investigate the effect of using Radial Jet Drilling (RJD) to create lateral micro-holes from vertical well completions in a fractured geothermal reservoir. Several fracture cases with varying fracture density, connectivity and distribution has been investigated using a doublet well set-up. The effect of using RJD techniques to create small lateral micro-holes of varying lengths between 25 and 100 meters from a vertical main well on the cold waterfront breakthrough time, thermal draw down, the down hole pressures and the energy balance of the reservoir. For each fracture case several well locations have been investigated with varying connectivity to the fractures in the reservoir. The main conclusions of the study is listed below.

- Adding lateral micro-holes to a set of vertical wells no matter the length of the laterals, or the placement of the wells relative to the fractures have no significant effect on the thermal breakthrough time or the thermal draw down of the reservoir. So, we can't expect an increase in the produced amount of energy from a geothermal reservoir by using RJD.
- When using RJD to create lateral micro-holes from a vertical well have the potential to significantly increase the productivity/injectivity of the wells. This effect strongly depends on the well location relative to the fractures in the reservoir. When looking at the pressure distribution in the reservoir, especially around the wells, the high and low-pressure zones at the injection well and production well the area with pressures above and below the formation pressure becomes bigger, but the peak pressures becomes lower when using RJD. The effect increases with the length of the laterals.
- Due to the effect that the laterals potentially have on the productivity and injectivity of the wells, an improvement in the net energy production from the reservoir is increased. This because the energy needed to sustain the down hole pressures is lower when the pressure difference is lower. This improves the energy balance of the system, and thereby increasing the profitable lifetime of the reservoir by several years.

The use of RJD to create lateral micro-holes from vertical well completions is shown to be a highly effective method to expand the high and low-pressure zones surrounding the injection well and production well, and lower the peak pressures in the reservoir. This means that the reservoir can be produced with down hole pressures closer to the formation pressure of the reservoir, and thereby dramatically lower the risk of damaging the formation with high injection pressures.
In cases where the produced hot water is used to generate electric power, the simulations done in this study indicated that the use of RJD has the potential to prolong the profitable lifetime of the reservoir by lowering the down hole pressures and thereby the energy needed to sustain set pressures, if the wells are located correctly relative to the fractures. In cases where the produced hot water is sent directly into the district heating system, the use of RJD won't be able to delay the cold waterfront breakthrough time, or slow the thermal draw down of the reservoir down. In this case the contribution from the lateral micro-holes will be to lower the operation cost of the system by lowering the energy needed by the pumps to sustain the flow.

6 Bibliography

[1] https://yearbook.enerdata.net/total-energy/world-consumption-statistics.html

[2] https://www.conserve-energy-future.com/geothermalenergyhistory.php

[3] https://yearbook.enerdata.net/total-energy/world-consumption-statistics.html

[4] http://petrowiki.org/Acid_fracturing

[5] https://www.studentenergy.org/topics/hydraulic-fracturing

[6] https://en.wikipedia.org/wiki/Hydraulic_fracturing

[7] http://petrowiki.org/Productivity_index_(J)

[8] https://en.wikipedia.org/wiki/Galerkin_method

[9] https://en.wikipedia.org/wiki/Finite_difference_method

[10] Bandis, S. C., A. C. Lumsden, and N. R. Barton. "Fundamentals of rock joint deformation." International Journal of Rock Mechanics and Mining Sciences & Geomechanics Abstracts. Vol. 20. No. 6. Pergamon, 1983.

[11] Barton, N., S. Bandis, and K. Bakhtar. "Strength, deformation and conductivity coupling of rock joints." International Journal of Rock Mechanics and Mining Sciences & Geomechanics Abstracts. Vol. 22. No. 3. Pergamon, 1985.

[12] Bodvarsson, Gunnar. "On the temperature of water flowing through fractures." Journal of Geophysical Research 74.8 (1969): 1987-1992.

[13] Buset, P., M. Riiber, and Arne Eek. "Jet drilling tool: cost-effective lateral drilling technology for enhanced oil recovery." SPE/ICoTA Coiled Tubing Roundtable. Society of Petroleum Engineers, 2001.

[14] Chi, Huanpeng, et al. "Maximum drillable length of the radial horizontal micro-hole drilled with multiple high-pressure water jets." Journal of Natural Gas Science and Engineering 26 (2015): 1042-1049.

[15] Chi, Huanpeng, et al. "Effects of the wellbore parameters of radial horizontal micro-holes on the gas reservoir production rate." Journal of Natural Gas Science and Engineering 24 (2015): 518-525.

[16] Crooijmans, R. A., et al. "The influence of facies heterogeneity on the doublet performance in low-enthalpy geothermal sedimentary reservoirs." Geothermics 64 (2016): 209-219.

[17] Crooijmans, R. A., et al. "The influence of facies heterogeneity on the doublet performance in low-enthalpy geothermal sedimentary reservoirs." Geothermics 64 (2016): 209-219.

[18] Ekneligoda, Thushan Chandrasiri, and Ki-Bok Min. "Determination of optimum parameters of doublet system in a horizontally fractured geothermal reservoir." Renewable energy 65 (2014): 152-160.

[19] Ghassemi, A., S. Tarasovs, and A. H-D Cheng. "An integral equation solution for three-dimensional heat extraction from planar fracture in hot dry rock." International Journal for Numerical and Analytical Methods in Geomechanics 27.12 (2003): 989-1004.

[20] Ghassemi, A., S. Tarasovs, and A. H-D Cheng. "An integral equation solution for three-dimensional heat extraction from planar fracture in hot dry rock." International Journal for Numerical and Analytical Methods in Geomechanics 27.12 (2003): 989-1004.

[21] Ghassemi, A., and X. Zhou. "A three-dimensional thermo-poroelastic model for fracture response to injection/extraction in enhanced geothermal systems." Geothermics 40.1 (2011): 39-49.

[22] Guo, Bin, et al. "Thermal drawdown-induced flow channeling in a single fracture in EGS." Geothermics 61 (2016): 46-62.

[23] Kohl, T., et al. "Coupled hydraulic, thermal and mechanical considerations for the simulation of hot dry rock reservoirs." Geothermics 24.3 (1995): 345-359.

[24] Liu, Yijun. "On the displacement discontinuity method and the boundary element method for solving 3-D crack problems." Engineering Fracture Mechanics 164 (2016): 35-45.

[25] McClure, Mark W., and Roland N. Horne. "An investigation of stimulation mechanisms in Enhanced Geothermal Systems." International Journal of Rock Mechanics and Mining Sciences 72 (2014): 242-260.

[26] Pandey, S. N., A. Chaudhuri, and S. Kelkar. "A coupled thermo-hydro-mechanical modeling of fracture aperture alteration and reservoir deformation during heat extraction from a geothermal reservoir." Geothermics 65 (2017): 17-31.

[27] Salimzadeh, Saeed, Adriana Paluszny, and Robert W. Zimmerman. "Three-dimensional poroelastic effects during hydraulic fracturing in permeable rocks." International Journal of Solids and Structures 108 (2017): 153-163.

[28] Sanyal, Subir K., and Steven J. Butler. "An analysis of power generation prospects from enhanced geothermal systems." Geothermal Resources Council Transactions 29 (2005): 131-8.

[29] Willems, C. J. L., et al. "The impact of reduction of doublet well spacing on the Net Present Value and the life time of fluvial Hot Sedimentary Aquifer doublets." Geothermics 68 (2017): 54-66.

7 Appendix A

7.1 Appendix A1

Here results from the (H) model simulations on the cases with a fracture aperture of $a_f = 9.68 \cdot 10^{-5}$ and $a_f = 4.93 \cdot 10^{-5}$ is shown.

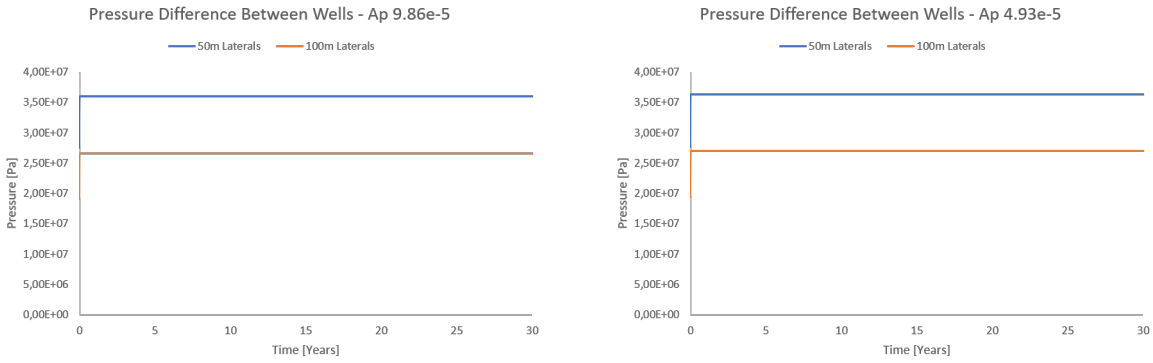

(a) (b)

Figure 36: (a) Pressure difference between the well for the $a_f = 9.86 \cdot 10^{-5}$ case with both 50 and 100 meter laterals. (b) Pressure difference between the well for the $a_f = 4.93 \cdot 10^{-5}$ case with both 50 and 100 meter laterals.

7.2 Appendix A2

Here results from the (TH) model simulations on the cases with a fracture aperture of $a_f = 9.68 \cdot 10^{-5}$ and $a_f = 4.93 \cdot 10^{-5}$ is shown.

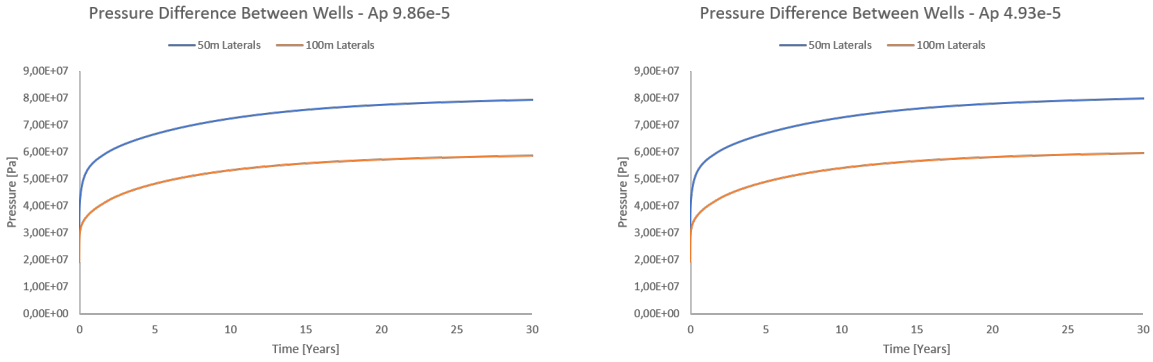

(a) (b)

Figure 37: (a) Pressure difference between the well for the $a_f = 9.86 \cdot 10^{-5}$ case with both 50 and 100 meter laterals. (b) Pressure difference between the well for the $a_f = 4.93 \cdot 10^{-5}$ case with both 50 and 100 meter laterals.

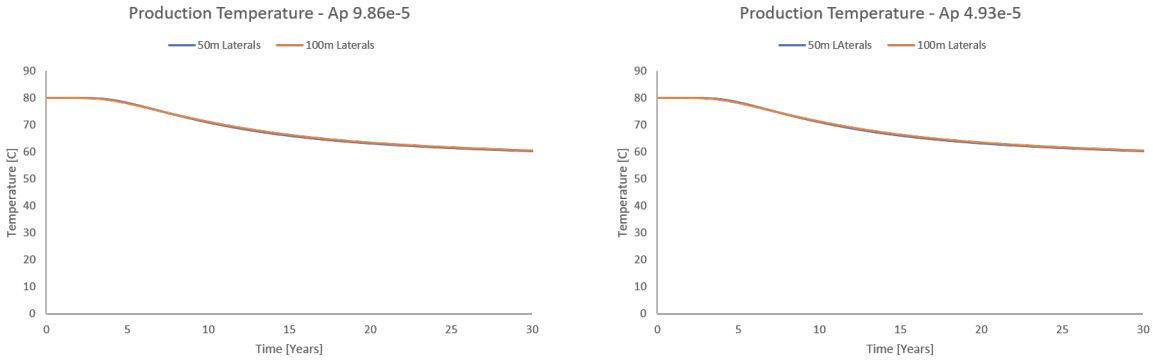

(a) (b)

Figure 38: (a) Production temperature profile for the $a_f = 9.86 \cdot 10^{-5}$ case with both 50 and 100 meter laterals. (b) Production temperature profile for the $a_f = 4.93 \cdot 10^{-5}$ case with both 50 and 100 meter laterals.

7.3 Appendix A3

Here results from the (THM) model simulations on the cases with a fracture aperture of $a_f = 9.68 \cdot 10^{-5}$ and $a_f = 4.93 \cdot 10^{-5}$ is shown.

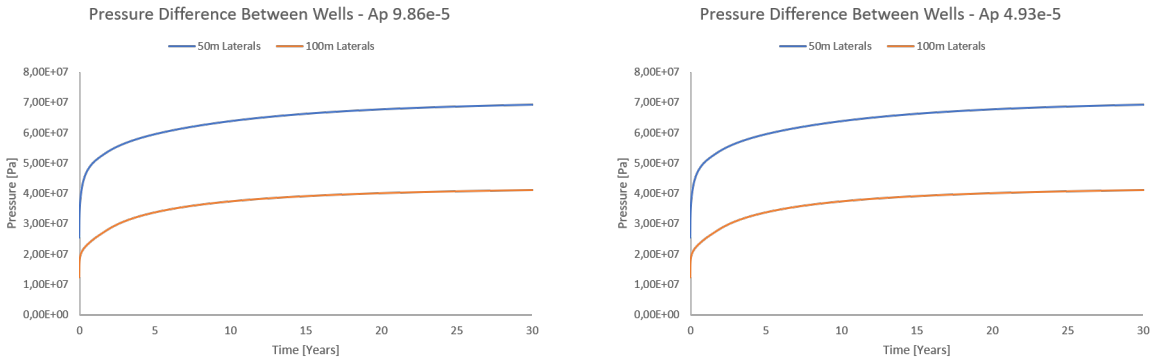

(a) (b)

Figure 39: (a) Pressure difference between the well for the $a_f = 9.86 \cdot 10^{-5}$ case with both 50 and 100 meter laterals. (b) Pressure difference between the well for the $a_f = 9.86 \cdot 10^{-5}$ case with both 50 and 100 meter laterals.

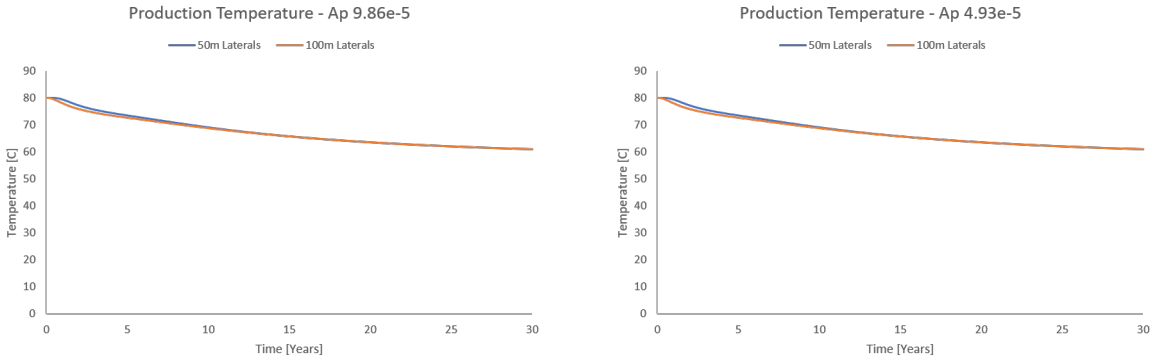

(a) (b)

Figure 40: (a) Production temperature profile for the $a_f = 9.86 \cdot 10^{-5}$ case with both 50 and 100 meter laterals. (b) Production temperature profile for the $a_f = 4.93 \cdot 10^{-5}$ case with both 50 and 100 meter laterals.

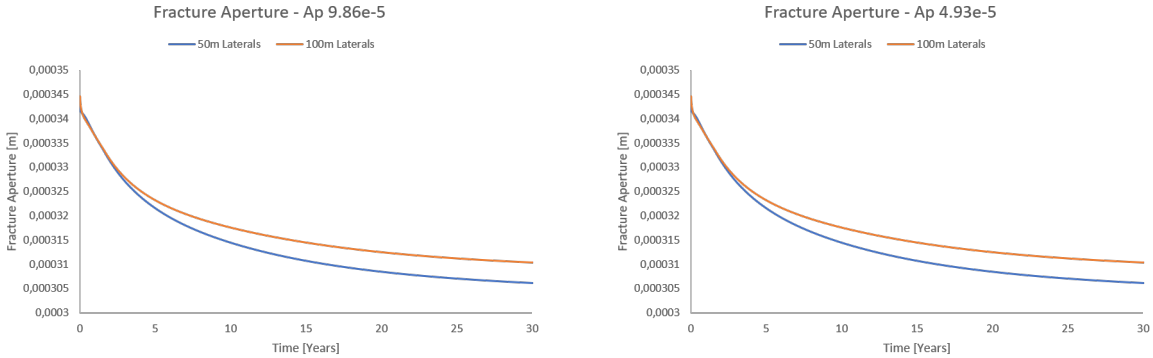

(a) (b)

Figure 41: (a) Average fracture aperture for the $a_f = 9.86 \cdot 10^{-5}$ case with both 50 and 100 meter laterals. (b) Average fracture aperture for the $a_f = 4.93 \cdot 10^{-5}$ case with both 50 and 100 meter laterals.

8 Appendix B

8.1 Appendix B1

1D permeability test for homogeneous fracture distribution with an initial fracture aperture of 0.2 millimetre.

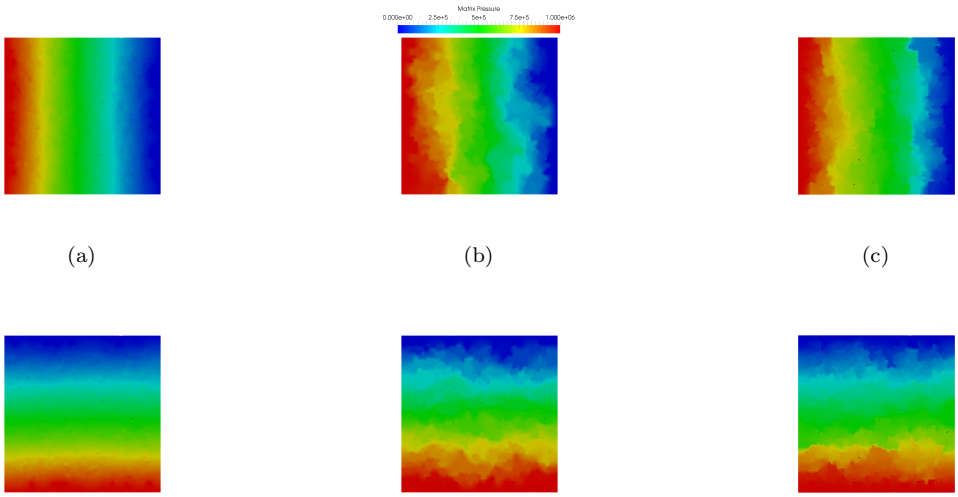

(a) (b) (c)

(d) (e) (f)

Figure 42: Matrix pressure in the reservoir when steady state flow conditions is reached using a TH model. On the top row the flow is in the x direction, and on the bottom row the flow is in the y direction. (a, d) Low fracture density. (b, e) Medium fracture density. (c, f) High fracture density.

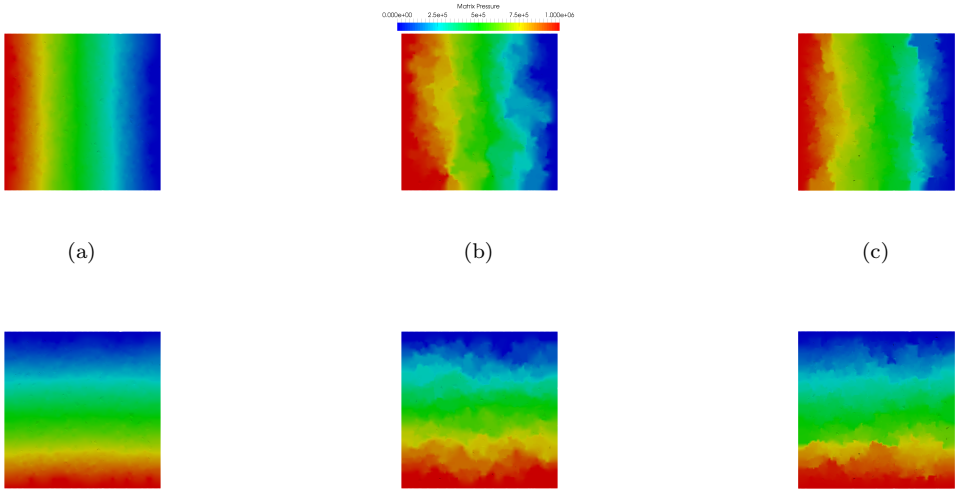

(a) (b) (c)

(d) (e) (f)

Figure 43: Matrix pressure in the reservoir when steady state flow conditions is reached using a THM model. On the top row the flow is in the x direction, and on the bottom row the flow is in the y direction. (a, d) Low fracture density. (b, e) Medium fracture density. (c, f) High fracture density.

8.2 Appendix B2

1D permeability test for heterogeneous fracture distribution with an initial fracture aperture of 0.2 millimetre.

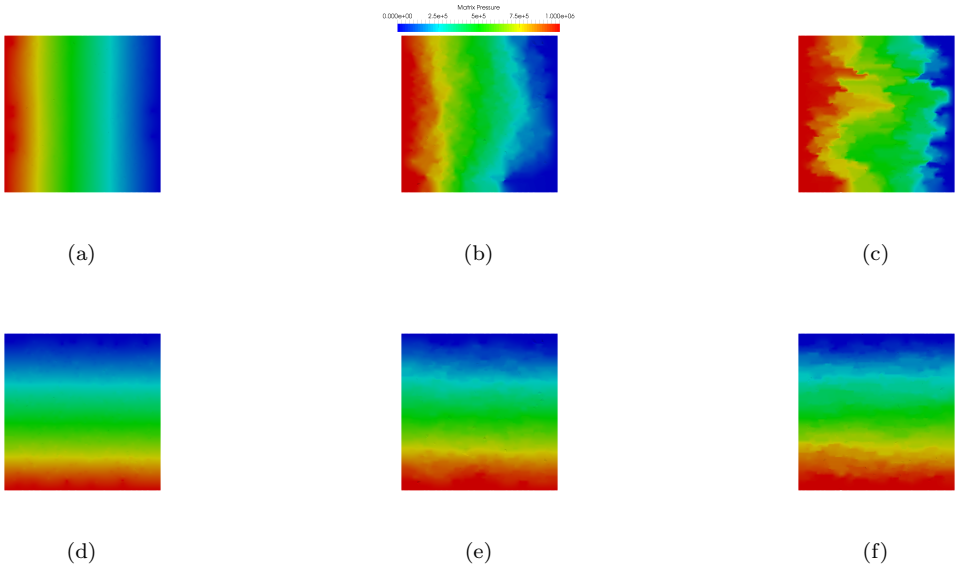

(a) (b) (c)

(d) (e) (f)

Figure 44: Matrix pressure in the reservoir when steady state flow conditions is reached using a TH model. On the top row the flow is in the x direction, and on the bottom row the flow is in the y direction. (a, d) Low fracture density. (b, e) Medium fracture density. (c, f) High fracture density.

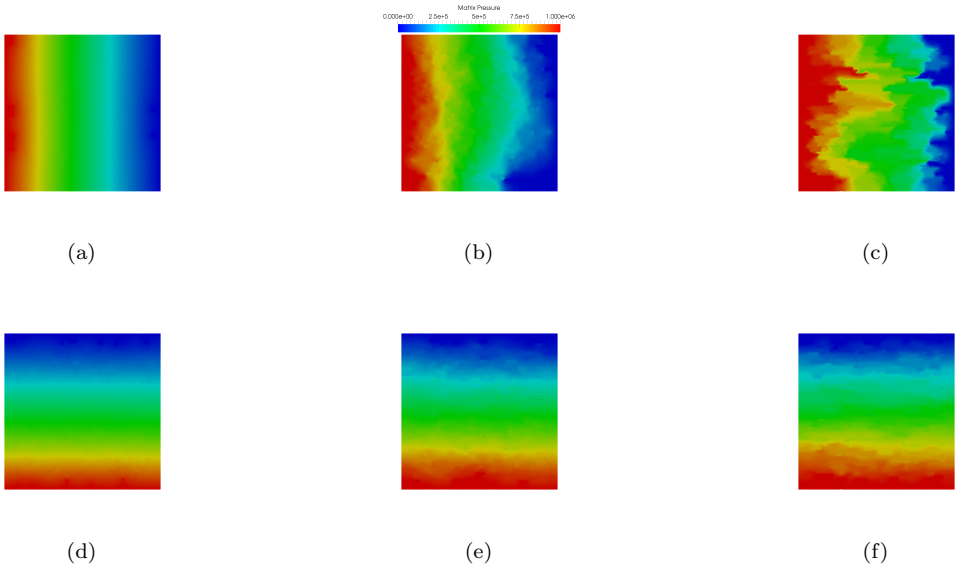

(a) (b) (c)

(d) (e) (f)

Figure 45: Matrix pressure in the reservoir when steady state flow conditions is reached using a THM model. On the top row the flow is in the x direction, and on the bottom row the flow is in the y direction. (a, d) Low fracture density. (b, e) Medium fracture density. (c, f) High fracture density.

8.3 Appendix B3

1D permeability test for long heterogeneous fracture distribution with an initial fracture aperture of 0.2 millimetre.

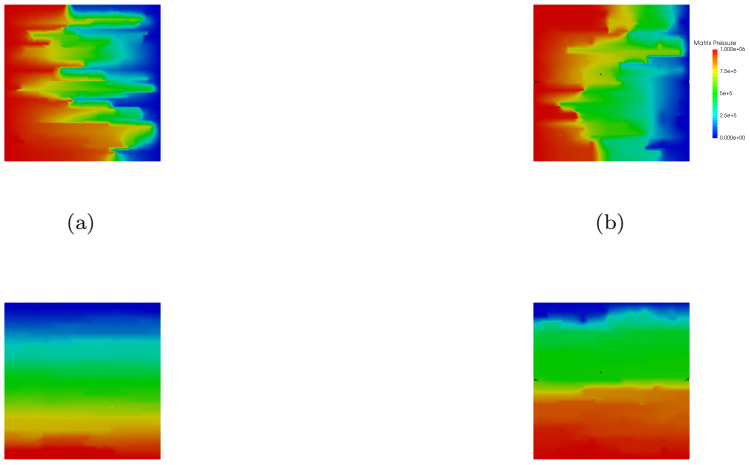

(a) (b)

(c) (d)

Figure 46: Matrix pressure in the reservoir when steady state flow conditions is reached using a TH model. On the top row the flow is in the x direction, and on the bottom row the flow is in the y direction. (a, c) non connected fracture case. (b, d) Connected fracture case.

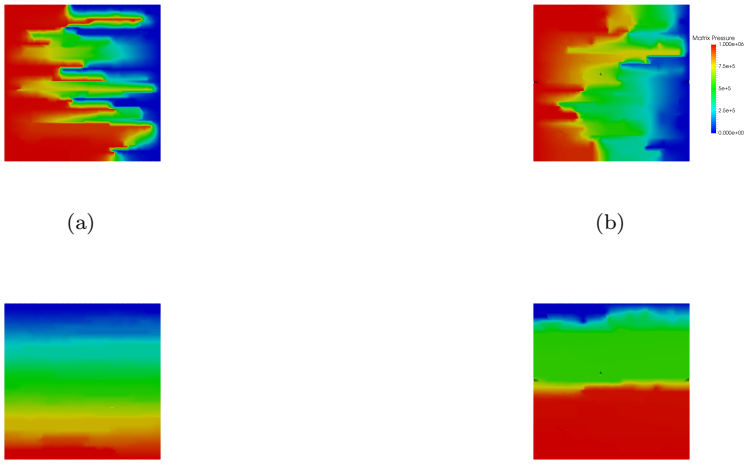

(a) (b)

(c) (d)

Figure 47: Matrix pressure in the reservoir when steady state flow conditions is reached using a THM model. On the top row the flow is in the x direction, and on the bottom row the flow is in the y direction. (a, c) non connected fracture case. (b, d) Connected fracture case.

9 Appendix C

9.1 Appendix C1

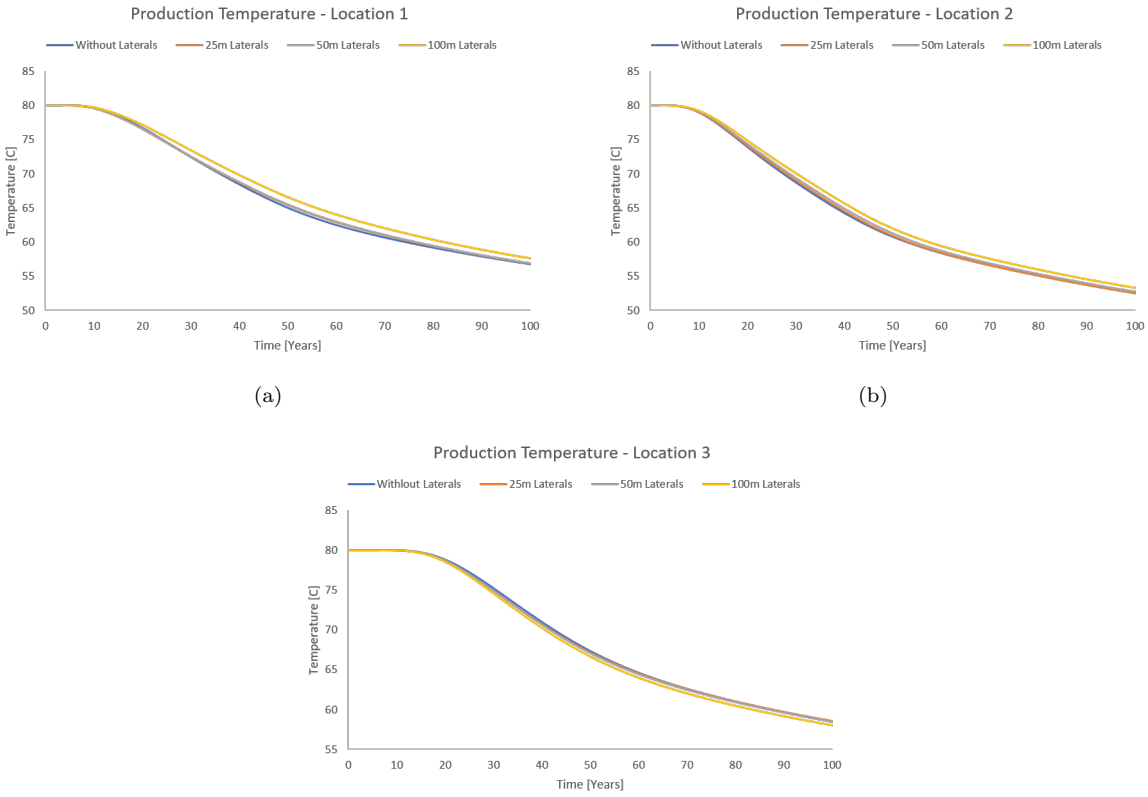

Figure 48: Production temperature profile for the medium fracture density fracture set with homogeneous fracture distribution for three well locations. (a) Wells placed in the matrix far away form the fractures in the reservoir. (b) Wells placed closer to the fractures in the reservoir, but not connected. (c) Wells connected to the fractures in the reservoir.

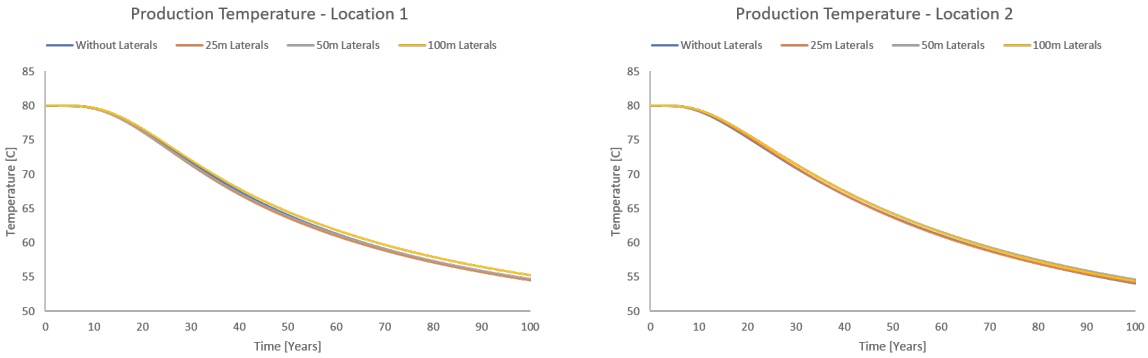

(a)

(b)

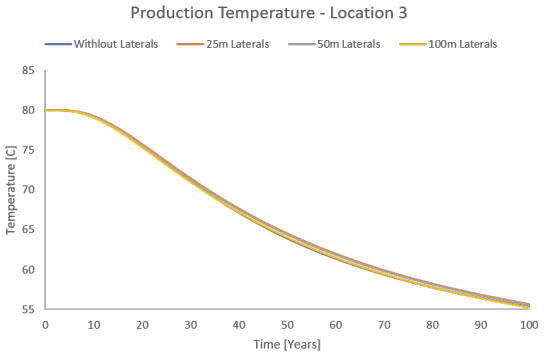

(c)

Figure 49: Production temperature profile for the high fracture density fracture set with homogeneous fracture distribution for three well locations. (a) Wells placed in the matrix far away form the fractures in the reservoir. (b) Wells placed closer to the fractures in the reservoir, but not connected. (c) Wells connected to the fractures in the reservoir.

9.2 Appendic C2

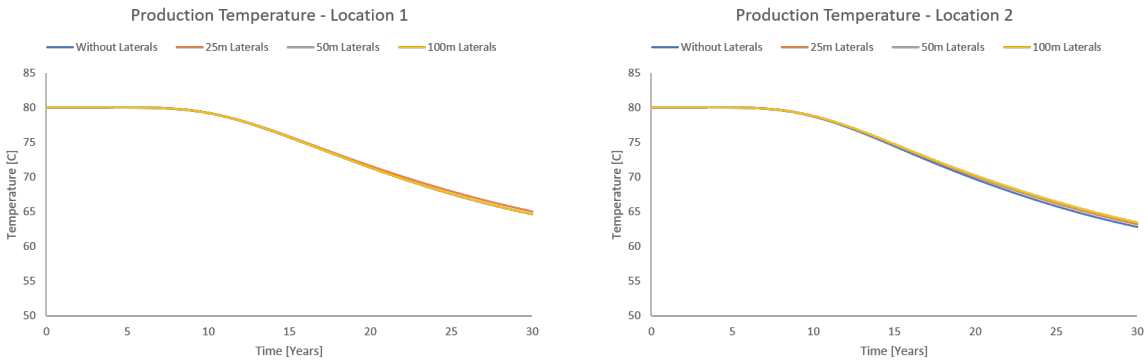

(a)

(b)

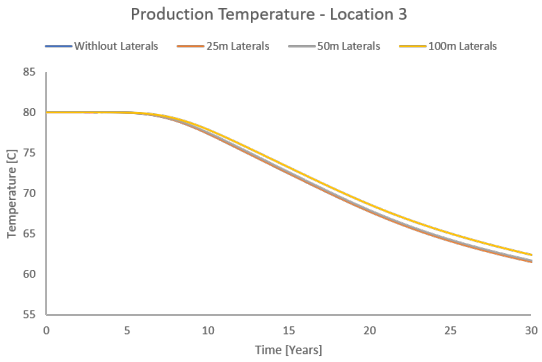

(c)

Figure 50: Production temperature profile for the medium fracture density fracture set with heterogeneous fracture distribution for three well locations. (a) Wells placed in the matrix far away form the fractures in the reservoir. (b) Wells placed closer to the fractures in the reservoir, but not connected. (c) Wells connected to the fractures in the reservoir.

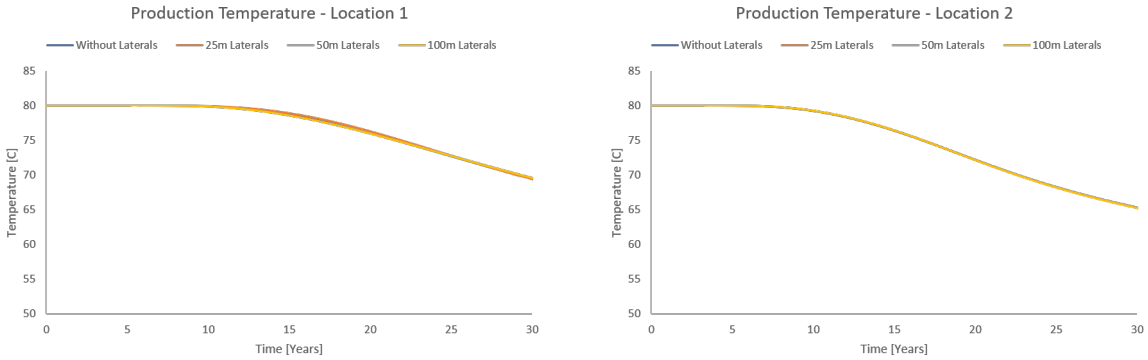

(a)

(b)

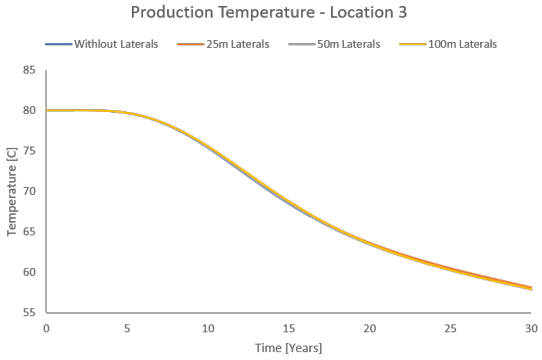

(c)

Figure 51: Production temperature profile for the high fracture density fracture set with heterogeneous fracture distribution for three well locations. (a) Wells placed in the matrix far away form the fractures in the reservoir. (b) Wells placed closer to the fractures in the reservoir, but not connected. (c) Wells connected to the fractures in the reservoir.

9.3 Appendix C3

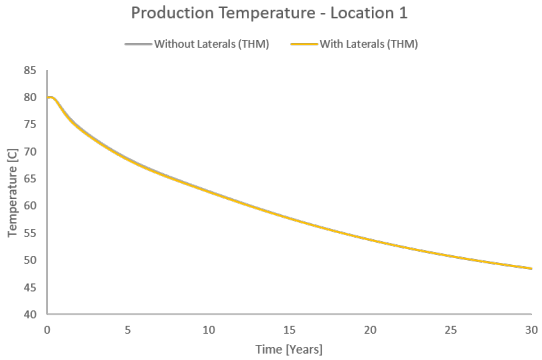

(a)

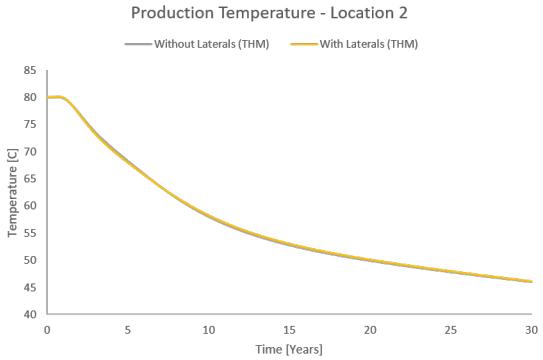

(b)

Figure 52: Production temperature profile for the high fracture density fracture set with long heterogeneous fracture distribution for three well locations. (a) Wells placed in the matrix far away form the fractures in the reservoir. (b) Wells connected to the fractures in the reservoir.

10 Appendix D

10.1 Appendix D1

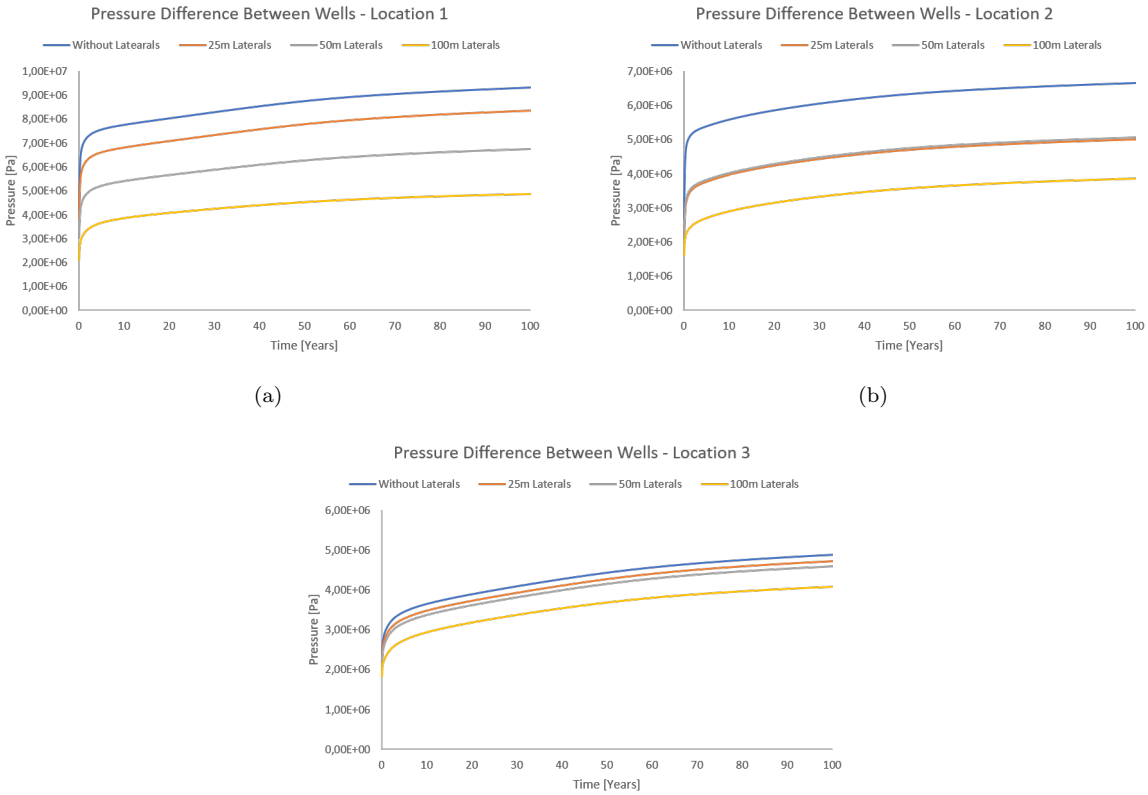

Figure 53: Pressure difference Between the injection well and the production well for the medium fracture density fracture set with homogeneous fracture distribution for three well locations. (a) Wells placed in the matrix far away form the fractures in the reservoir. (b) Wells placed closer to the fractures in the reservoir, but not connected. (c) Wells connected to the fractures in the reservoir.

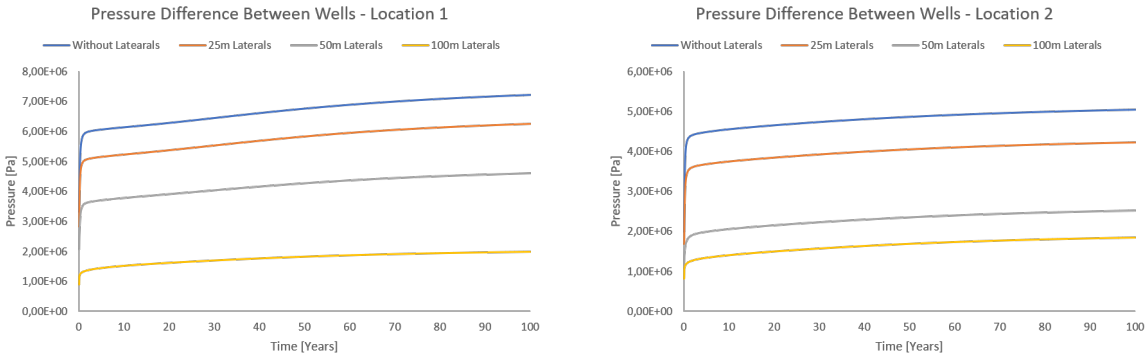

(a)

(b)

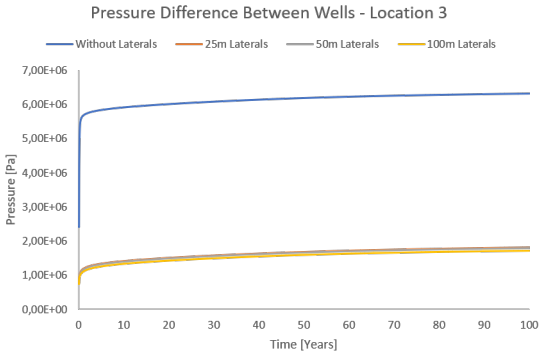

(c)

Figure 54: Pressure difference Between the injection well and the production well for the high fracture density fracture set with homogeneous fracture distribution for three well locations. (a) Wells placed in the matrix far away form the fractures in the reservoir. (b) Wells placed closer to the fractures in the reservoir, but not connected. (c) Wells connected to the fractures in the reservoir.

10.2 Appendix D2

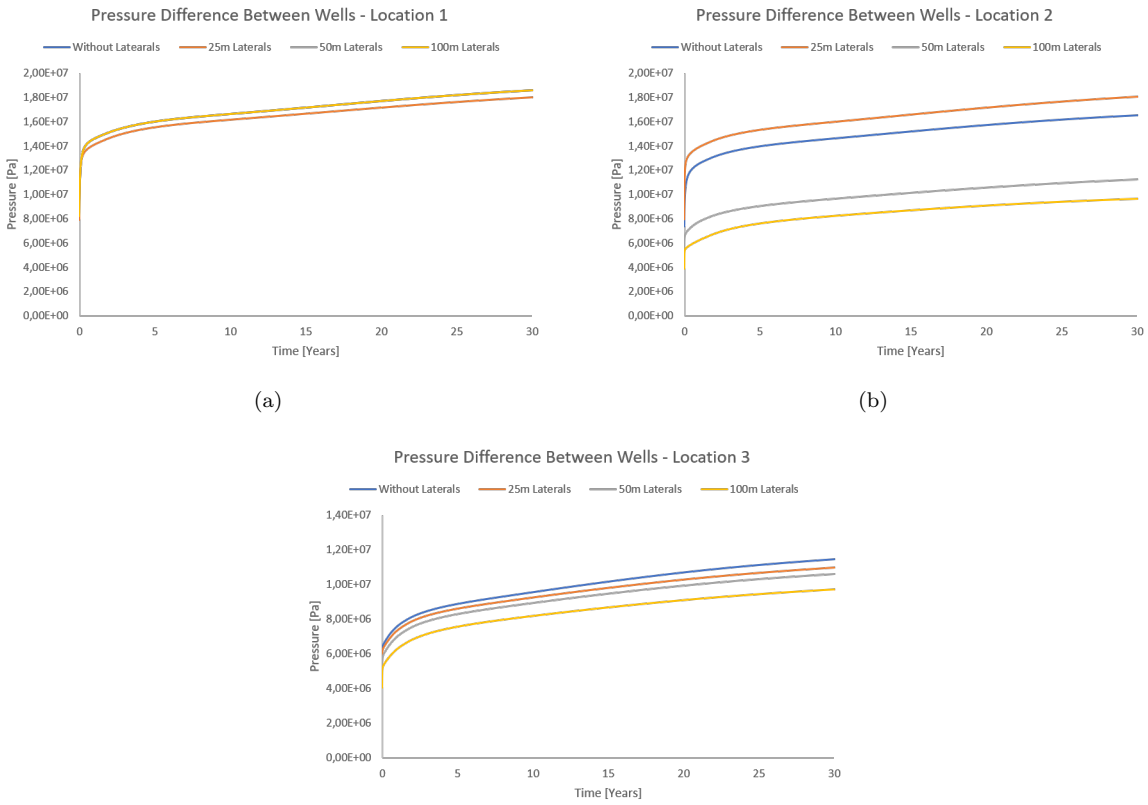

Figure 55: Pressure difference Between the injection well and the production well for the medium fracture density fracture set with heterogeneous fracture distribution for three well locations. (a) Wells placed in the matrix far away form the fractures in the reservoir. (b) Wells placed closer to the fractures in the reservoir, but not connected. (c) Wells connected to the fractures in the reservoir.

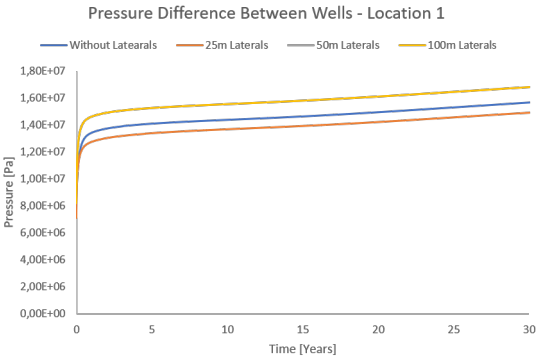

(a)

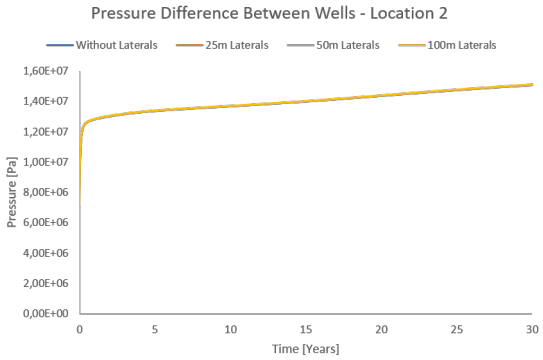

(b)

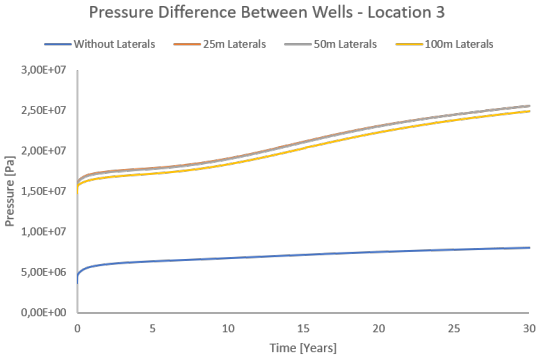

(c)

Figure 56: Pressure difference Between the injection well and the production well for the high fracture density fracture set with heterogeneous fracture distribution for three well locations. (a) Wells placed in the matrix far away form the fractures in the reservoir. (b) Wells placed closer to the fractures in the reservoir, but not connected. (c) Wells connected to the fractures in the reservoir.

10.3 Appendix D3

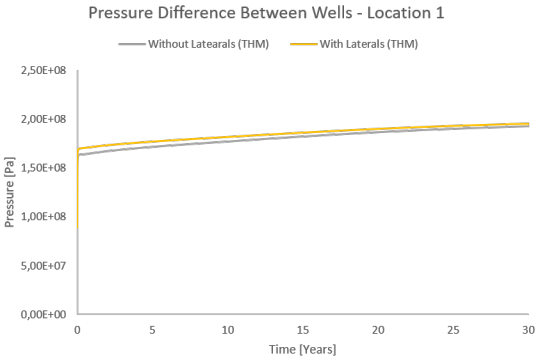

(a)

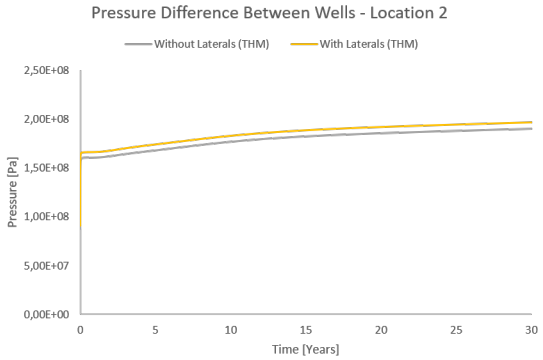

(b)

Figure 57: Pressure difference Between the injection well and the production well for the high fracture density fracture set with long heterogeneous fracture distribution for three well locations. (a) Wells placed in the matrix far away form the fractures in the reservoir. (b) Wells connected to the fractures in the reservoir.

11 Appendix E

11.1 Appendix E1

Here results on the net energy produced for a medium and highly fractured reservoir shown on figures 58 and 59, respectivly. In this case the reservoirs is produced to the point where the production temperature becomes $65°C$.

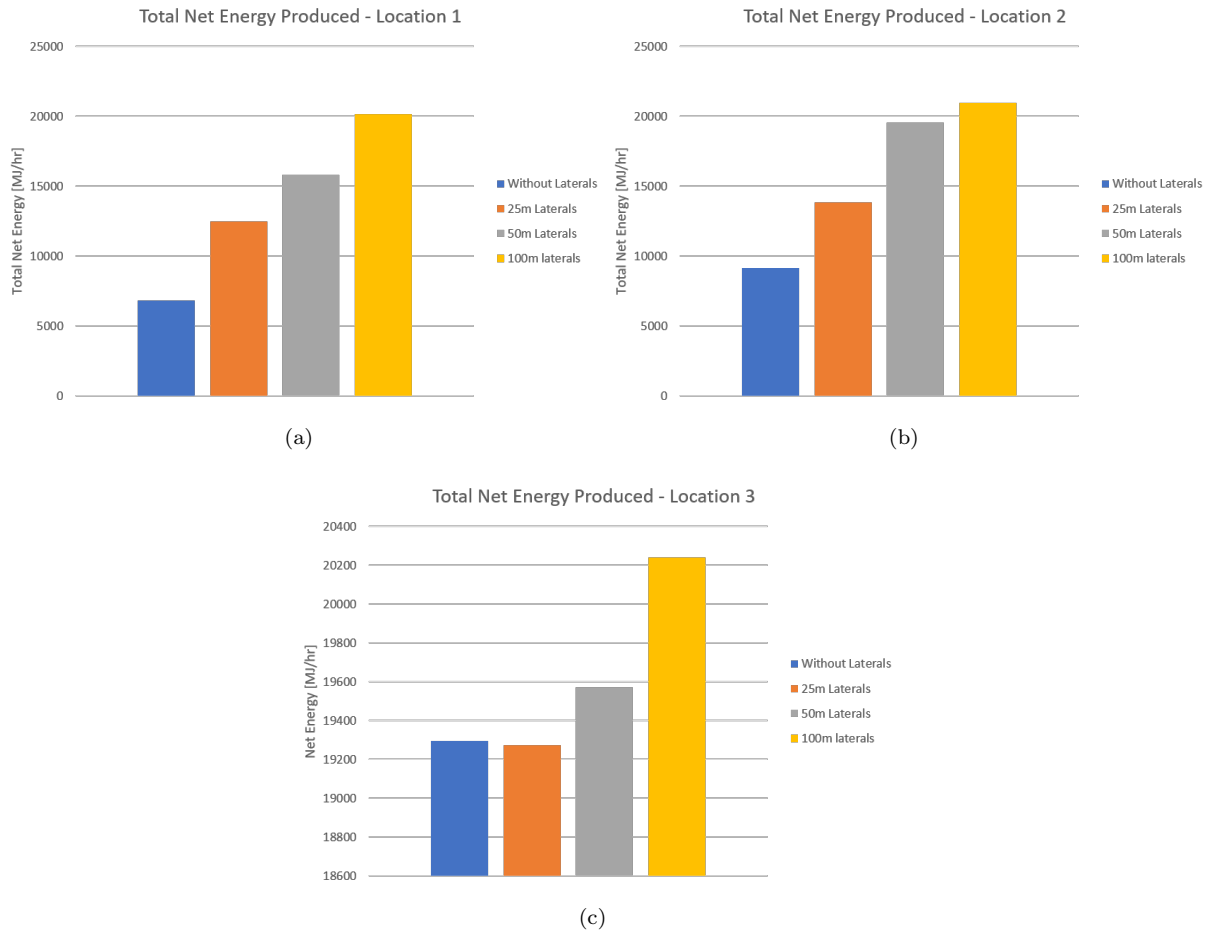

Figure 58: Total amount of net energy for a geothermal reservoir when the reservoir is produced to an abandonment time of $LT = 65°C$. The reservoir has a medium fracture permeability and connectivity for different well locations. (a) Well placed in the matrix away from the fracture network. (b) Well placed in the matrix but close to the fracture network. (c) Well placed so the intersect the fracture network.

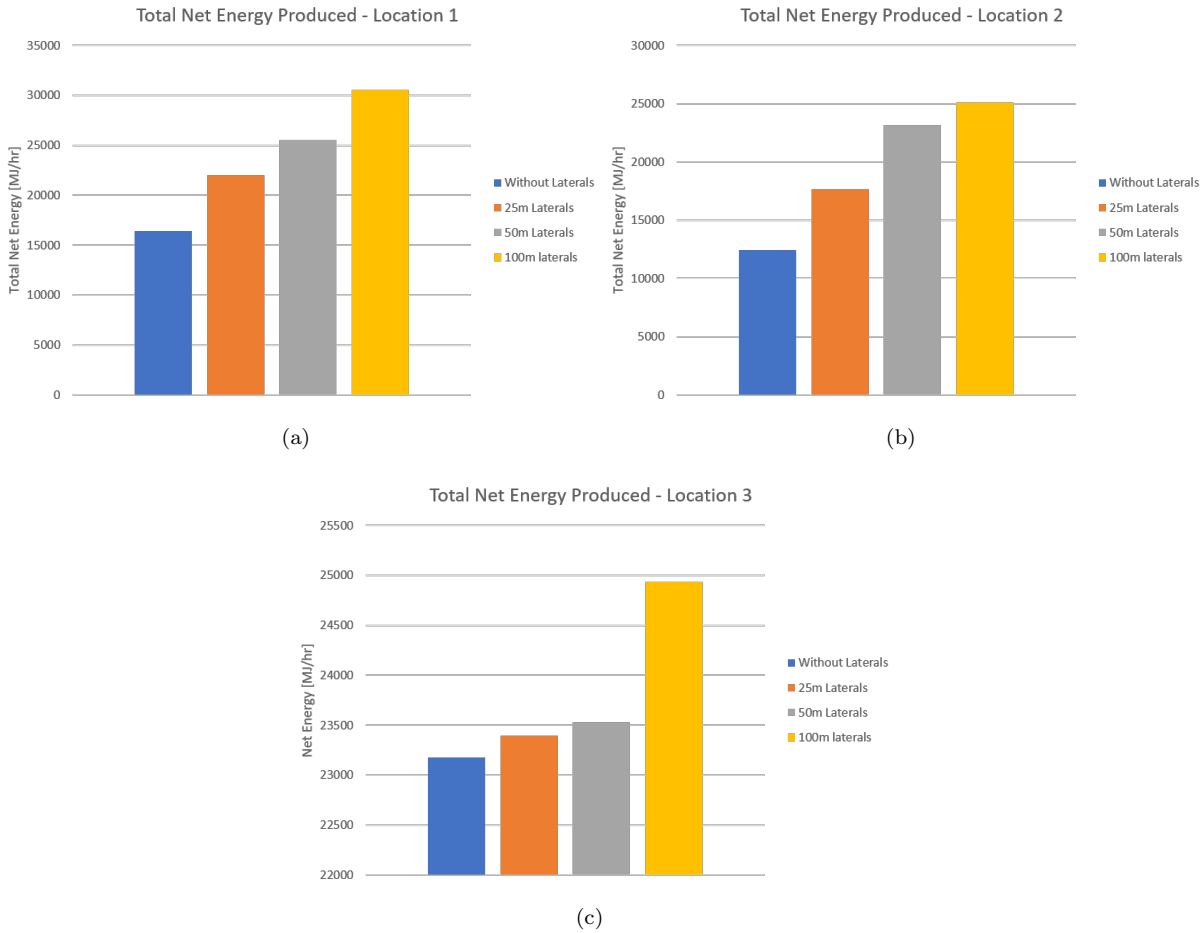

Figure 59: Total amount of net energy for a geothermal reservoir when the reservoir is produced to an abandonment time of $LT = 65°C$. The reservoir has a high fracture permeability and connectivity for different well locations. (a) Well placed in the matrix away from the fracture network. (b) Well placed in the matrix but close to the fracture network. (c) Well placed so the intersect the fracture network.

11.2 Appendix E2

Here the results from figures 58 and 59 is presented as a function of production time, instead of total amount of net energy produced.

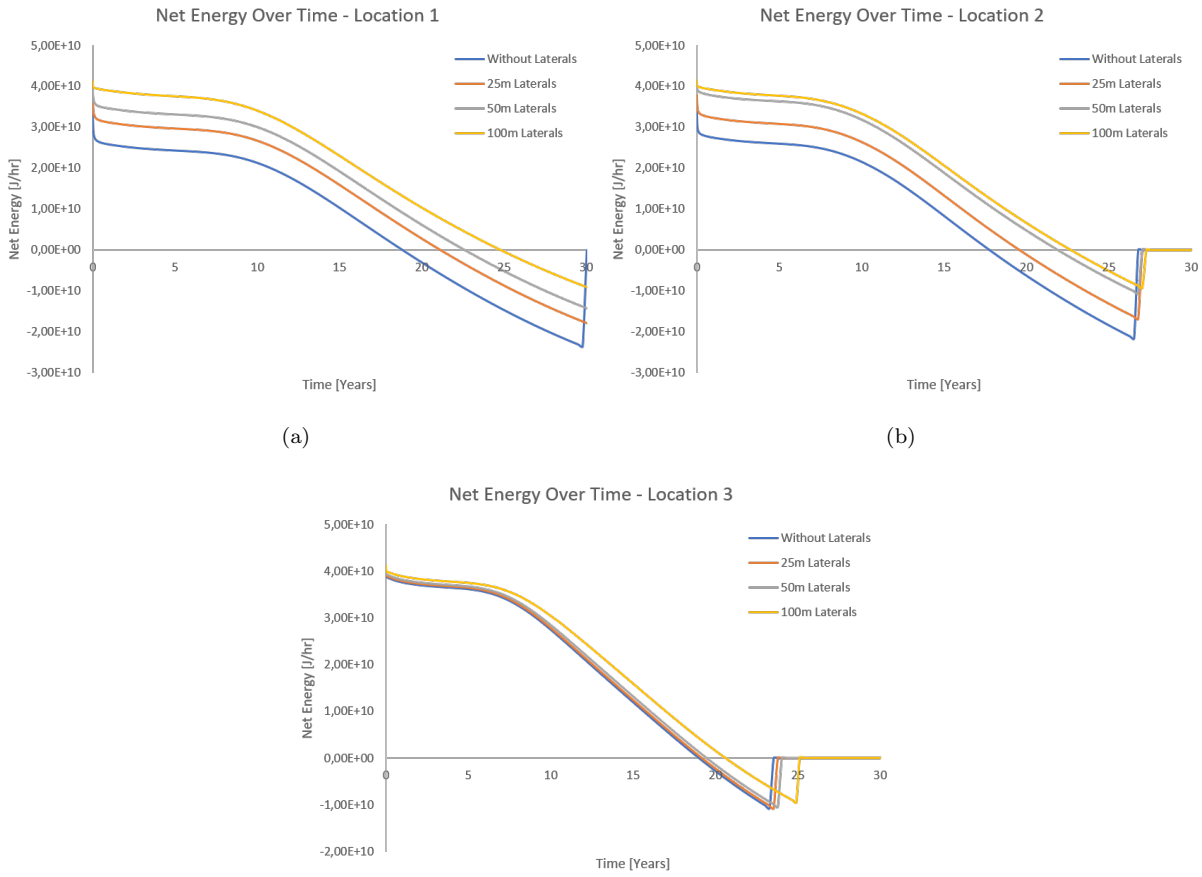

(a) (b)

(c)

Figure 60: The same trend is seen here for the reservoir with medium fracture density. The net energy becomes negative in the late part of the production period. This again indicates the importances of the abandonment time for optimal energy recovery.

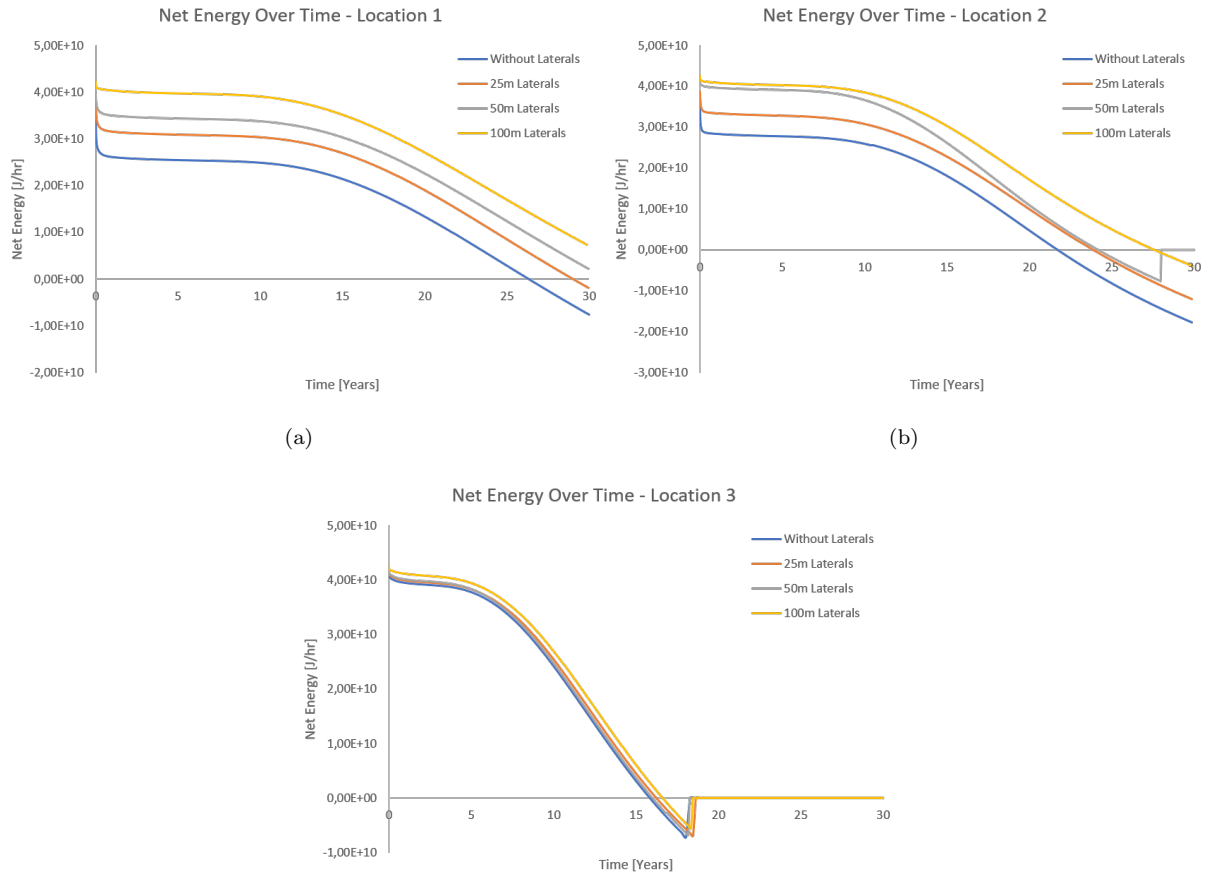

Figure 61: The same trend is seen here for the reservoir with high fracture density. The net energy becomes negative in the late part of the production period. This again indicates the importances of the abandonment time for optimal energy recovery.

11.3 Appendix E3

When using the information obtained on figures 60 and 61 the optimal amount of net energy produced can be fund. This is shown on figures 62 and 63.

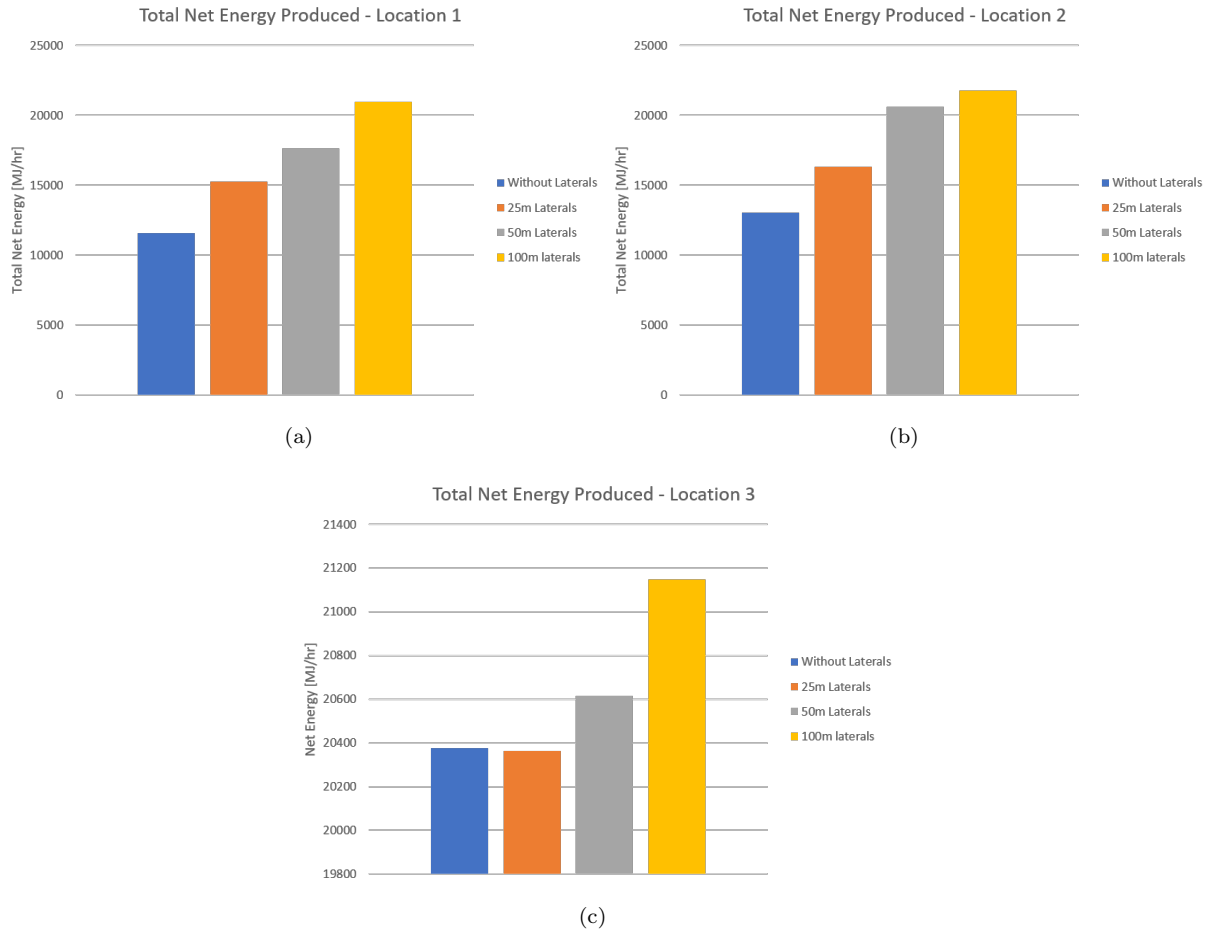

Figure 62: The optimal amount of net energy produced from the reservoir with medium fracture density.

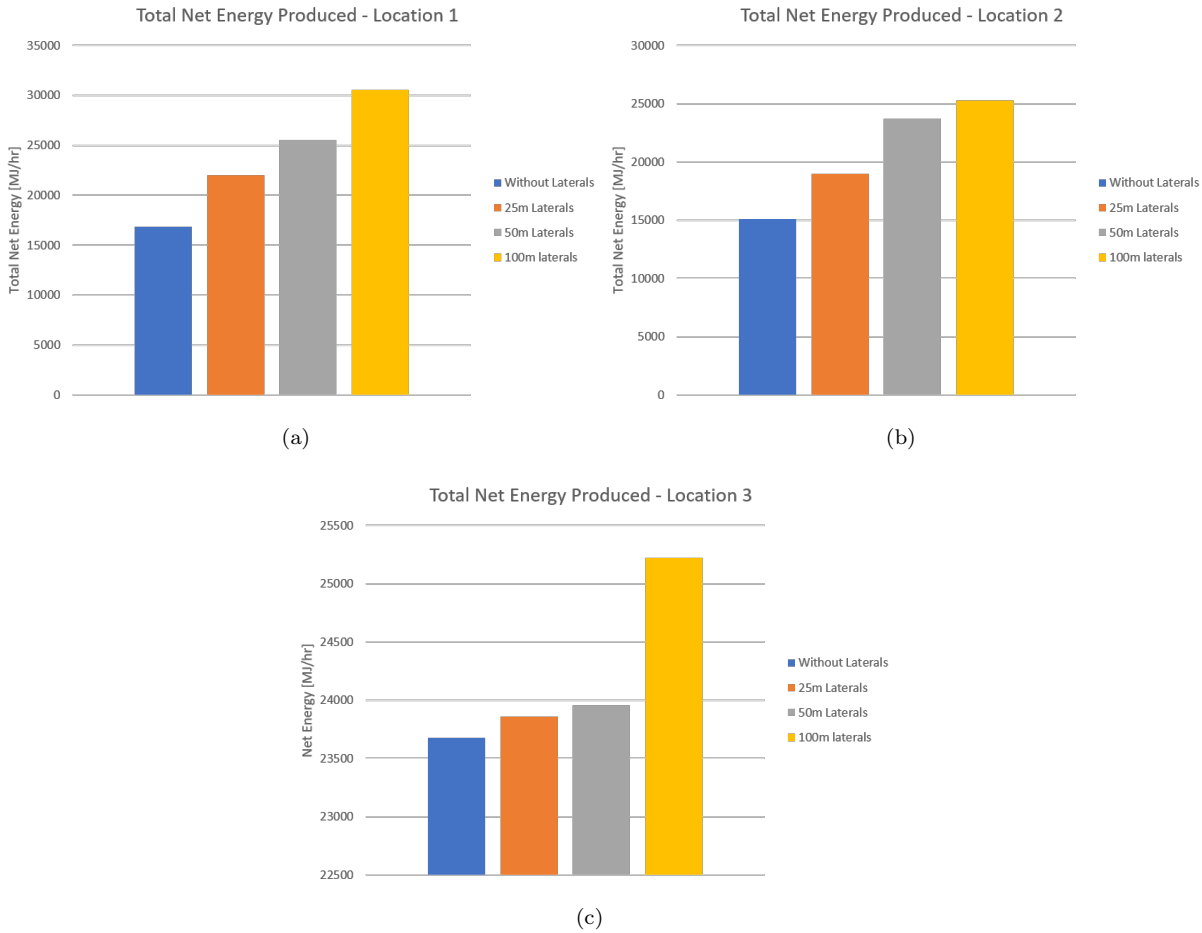

Figure 63: The optimal amount of net energy produced from the reservoir with high fracture density.